

## REMNANT OF A “WET” MERGER: NGC 34 AND ITS YOUNG MASSIVE CLUSTERS, YOUNG STELLAR DISK, AND STRONG GASEOUS OUTFLOW<sup>1</sup>

FRANÇOIS SCHWEIZER

Carnegie Observatories, 813 Santa Barbara Street, Pasadena, CA 91101; schweizer@ociw.edu

AND

PATRICK SEITZER

Department of Astronomy, University of Michigan, 818 Dennison Building,  
Ann Arbor, MI 48109; pseitzer@umich.edu

To appear in *The Astronomical Journal*, Vol. 133

### ABSTRACT

This paper presents new images and spectroscopic observations of NGC 34 (Mrk 938) obtained with the du Pont 2.5-m and Baade 6.5-m telescopes at Las Campanas, plus photometry of an archival  $V$  image obtained with *Hubble Space Telescope*. This  $M_V = -21.6$  galaxy has often been classified as a Seyfert 2, yet recently published infrared spectra suggest a dominant central starburst. We find that the galaxy features a single nucleus, a main spheroid containing a blue central disk and much outer fine structure, and tidal tails indicative of two former disk galaxies. At present these galaxies appear to have completed merging. The remnant shows three clear optical signs that the merger was gas-rich (“wet”) and accompanied by a starburst: (1) It sports a rich system of young star clusters, of which 87 have absolute magnitudes  $-10.0 \geq M_V \geq -15.4$ . Five clusters with available spectra have ages in the range 0.1–1.0 Gyr and photometric masses of  $2 \times 10^6 \lesssim M \lesssim 2 \times 10^7 M_\odot$ ; they are gravitationally bound young globulars. (2) The blue central disk appears to be young. It is exponential, can be traced to  $\gtrsim 10$  kpc radius, and has a smooth structure and colors suggesting that its optical light is dominated by a  $\sim 400$  Myr old poststarburst population. And (3), the center of NGC 34 drives a strong outflow of cool, neutral gas, as revealed by broad blueshifted Na I D-lines. The center-of-line velocity of this gas is  $-620$  km s<sup>-1</sup>, while the maximum detected outflow velocity reaches  $-1050$  km s<sup>-1</sup>. Assessing all available evidence, we suggest that NGC 34 stems from two recently merged gas-rich disk galaxies with an estimated mass ratio of  $1/3 \lesssim m/M \lesssim 2/3$ . The remnant seems to have first experienced a galaxy-wide starburst that then shrank to its current central and obscured state. The strong gaseous outflow came last.

*Subject headings:* galaxies: evolution — galaxies: formation — galaxies: individual (NGC 34, NGC 17, Mrk 938) — galaxies: interactions — galaxies: star clusters — galaxies: structure

### 1. INTRODUCTION

Over the past decade it has become widely accepted that hierarchical mergers play an important role in galaxy evolution (White & Rees 1978). Most such mergers involve gas and the formation of stars since, even at the present epoch, the great majority of galaxies contain cold gas (Toomre & Toomre 1972; Larson & Tinsley 1978; Schweizer 1983). Thus, gas-rich, “wet” mergers are an integral part of galaxy formation and growth (Barnes & Hernquist 1992, 1996; Mihos & Hernquist 1996). Many interesting processes occur during these mergers, leading to phenomena such as starbursts and active galactic nuclei (AGN).

Whereas star and star-cluster formation during merger-induced starbursts are beginning to be better understood, the processes associated with the formation and growth of central black holes, and with their feedback on the surrounding gas, remain mysterious (e.g., Springel et al. 2005). Yet, the existence of a strong correlation between black-hole mass and spheroid mass (Ferrarese & Merritt 2000; Gebhardt et al. 2000; Tremaine et al. 2002) compels us to believe that, no matter what the details of gas-rich mergers and accretions, the physical processes dictating black-hole growth may be surprisingly uniform and well defined (Hopkins et al. 2006).

Some questions of interest are: What is the sequence of events leading up to the formation of a central starburst and

AGN? When does gaseous outflow begin and when does it peak? And what are the conditions under which quenching of further star formation may occur? Observational answers to these questions can be sought through statistical studies of large samples of relatively distant objects or through more detailed studies of individual nearby mergers and merger remnants, where the relevant processes can be observed in detail.

The present paper takes the latter approach and addresses mainly the first two of the above questions. The galaxy NGC 34 was first pointed out to us as a likely merger remnant by Dr. Christopher Mihos. It is a relatively nearby representative of the class of Luminous Infrared Galaxies (LIRGs)—defined as having infrared luminosities  $L_{\text{IR}}$  (from  $\sim 8$ – $1300$   $\mu\text{m}$ ) in the range  $11.0 \leq \log(L_{\text{IR}}/L_\odot) < 12.0$  (Soifer et al. 1987)—and has, therefore, been studied extensively in the infrared. Its logarithmic infrared luminosity of  $\log(L_{\text{IR}}/L_\odot) = 11.54$  (Chini et al. 1992) places it in the mid-range of this class.<sup>2</sup> The galaxy has been noted for its exceptionally high central luminosity density in the  $H$  passband (van der Marel & Zurek 2000; Mihos 2001) and has recently attracted attention for its feature-rich IR spectrum. In the near IR (0.8–2.4  $\mu\text{m}$ ), relatively weak forbidden emission lines from [C I], [S III], and [Fe II] are present in addition to the usual permitted lines of H I, H<sub>2</sub>, and He I (Riffel et al. 2006),

<sup>2</sup> Smaller values of  $\log(L_{\text{IR}}/L_\odot) \approx 11.3$ – $11.4$  are often quoted for NGC 34, but are usually based only on the 60  $\mu\text{m}$  and 100  $\mu\text{m}$  fluxes observed by *IRAS*.

<sup>1</sup> Based in part on observations with the 6.5 m Magellan Telescopes located at Las Campanas Observatory, Chile.

while in the mid-IR (5–20  $\mu\text{m}$ ) the spectrum is dominated by strong emission lines from polycyclic aromatic hydrocarbons (PAHs) and a broad, deep Silicate absorption trough centered at  $\sim 10 \mu\text{m}$  (Buchanan et al. 2006). In fact, based on the latter features Buchanan et al. declare NGC 34 to be the archetype of a large group of (mostly Seyfert) galaxies with very red nuclear continua suggestive of cool dust and strong PAH emission lines.

The exact nature and origin of NGC 34’s *optical* nuclear spectrum have long been controversial. The present tendency is to place NGC 34 in a transition category of objects with nuclear spectra between starburst-dominated and of type Seyfert 2 (= Sey 2; e.g., Gonçalves et al. 1999). This transition category is occasionally called AMB for “ambiguous” (e.g., Corbett et al. 2003).

In the past, many observers have classified NGC 34 as a Sey 2 (e.g., Afanasev et al. 1980; Dahari 1985; Véron-Cetty & Véron 1986; Goldader et al. 1997a). Yet, others have emphasized the apparent weakness of the [O III]  $\lambda 5007$  emission line relative to either H $\beta$  or H $\alpha$  and have classified NGC 34 as a narrow-emission-line galaxy (Osterbrock & Dahari 1983; Veilleux & Osterbrock 1987; Goldader et al. 1997b) or starburst galaxy (e.g., Mazzarella et al. 1991; Mazzarella & Boroson 1993; Mulchaey et al. 1996; near IR: Riffel et al. 2006). In one illustrative example of the ambivalence of spectral classifiers, Véron-Cetty & Véron (1986) describe NGC 34 as “indeed a Seyfert 2 galaxy” based on their ESO 3.6-m telescope CCD spectrum, yet display this spectrum under the non-Seyfert category “Miscellaneous” and label it with “H II” (for starburst).

Modern studies of the possible compositeness of NGC 34’s nuclear spectrum have led to estimates for the relative contributions to the bolometric flux of the starburst and AGN ranging between about 75%/25% (Imanishi & Alonso-Herrero 2004) and 90%/10% (Gonçalves et al. 1999). What all modern studies involving infrared flux measurements agree on is that the central star formation rate (SFR) in NGC 34 is high, with estimates ranging from about  $50 M_{\odot} \text{ yr}^{-1}$  (Valdes et al. 2005) to  $80\text{--}90 M_{\odot} \text{ yr}^{-1}$  (Prouton et al. 2004).

There is independent evidence for the likely presence of an AGN in NGC 34 from the measured X-ray luminosity which, corrected for strong and uncertain absorption, is  $L_{X, 2\text{--}10\text{keV}} \approx 2.2_{-0.9}^{+2.8} \times 10^{42} \text{ erg s}^{-1}$  (Guainazzi et al. 2005; 1- $\sigma$  errors computed by Dr. Jane Rigby, private commun.). This luminosity, measured from *XMM-Newton* observations, is comparable to that of the classical Seyfert 1.5 galaxy NGC 4151 and is too high to be explained in terms of a pure starburst and its associated X-ray binaries. Thus, it seems to support the presence of a weak AGN, even though there is no high-resolution observation by *Chandra* to directly confirm the presence of a dominant central X-ray point source.

NGC 34 is definitely gas rich and can, therefore, sustain its strong central starburst and present mild AGN activity for some time to come. Compilations of available measurements yield a neutral-hydrogen gas mass of  $M_{\text{HI}} \approx 5.3 \times 10^9 M_{\odot}$  (Kandalyan 2003) and a molecular-gas mass (from CO observations) of  $M_{\text{H}_2} = (7 \pm 3) \times 10^9 M_{\odot}$  (Kandalyan 2003; Krügel et al. 1990; Chini et al. 1992). Both mass values have been adjusted to the distance scale adopted here ( $H_0 = 70$ , see below).

The galaxy NGC 34 is also known as NGC 17, Mrk 938, VV 850, MCG–02-01-032, IRAS F0085–1223, and 2MASX

J00110661–1206283. It is located at  $\alpha_{J2000} = 00^{\text{h}}11^{\text{m}}06^{\text{s}}54$ ,  $\delta_{J2000} = -12^{\circ}06'27''.4$  (see § 3.1) and has a recession velocity relative to the Local Group of  $c_{z_{\text{LG}}} = +5961 \pm 15 \text{ km s}^{-1}$  (§ 3.3), which places it at a distance of 85.2 Mpc for  $H_0 = 70 \text{ km s}^{-1} \text{ Mpc}^{-1}$ . At that distance, adopted throughout the present paper,  $1'' = 413 \text{ pc}$ . The corresponding true distance modulus is  $(m - M)_0 = 34.65$ . The Milky Way foreground extinction is small, with values in the literature ranging between  $A_V = 0.053$  (de Vaucouleurs et al. 1991) and 0.089 (Schlegel, Finkbeiner, & Davis 1998). We adopt the latter value, with which the absolute visual magnitude of NGC 34 becomes  $M_V = -21.57$  (§ 3.3).

In the following, § 2 describes the observations and reductions, including imaging, aperture and surface photometry, and spectroscopy. Section 3 presents results concerning the morphology and photometric structure of NGC 34, its nuclear spectrum, and its system of young massive clusters. Section 4 then discusses the structure and nature of this galaxy as a likely remnant of a “wet” unequal-mass merger, the nature of its clusters, and the properties of its gaseous outflow. Finally, § 5 summarizes our main conclusions.

## 2. OBSERVATIONS AND REDUCTIONS

The observations of NGC 34 described in the present paper include a series of *BVI* exposures obtained with the direct CCD camera of the Irénée du Pont 2.5-m telescope at Las Campanas Observatory, an archival *V* image taken with the Wide Field and Planetary Camera 2 (WFPC2) of the *Hubble Space Telescope* (*HST*), and spectra of the nucleus and of five bright star clusters taken with the Low-Dispersion Survey Spectrograph (LDSS-2) of the Baade 6.5-m telescope at Las Campanas. Table 1 presents a log of these observations.

### 2.1. Imaging

Direct images of NGC 34 in *BVI* were obtained with the CCD camera of the du Pont 2.5-m telescope on 2000 Sep 30 (see Table 1). The camera was equipped with the chip Tek#5 (format  $2048 \times 2048$ ), which yielded a field of view of  $8'.9 \times 8'.9$  and a scale of  $0''.2607/\text{pixel}$ . A standard *UBVRI*<sub>KC</sub> filter set was used, with the *I*<sub>KC</sub> filter designed for the Kron-Cousins system and the corresponding passband hereafter called *I* for short. Conditions were photometric, and the seeing was in the range  $0''.7\text{--}0''.9$  (FWHM).

Figure 1 shows portions of the *B* image (Panels a–e) and *I* image (Panel f) at various contrasts, with scale bars indicating the angular and projected linear scales. The box in Fig. 1a identifies the area shown  $3\times$  enlarged in Figs. 1b–1f. Notice the two near-linear tidal tails to the NE and SW of the system and the various sharp-edged streamers, all typical of interacting and merging *disk* galaxies. A comparison of Figs. 1e and 1f shows that the general appearance of NGC 34 changes relatively little from *B* to *I*, but that the tidal features appear significantly brighter and more knotty in blue light (*B*).

A search of the *HST* Archive showed that, besides many NICMOS observations, a single optical broad-band image of NGC 34 existed (as of 2006 July 1). This image, obtained during *HST* Cycle 5 with the WFPC2 camera and single-star guidance (GO-5479, PI: M. Malkan), is a 500 s exposure through the F606W filter; it was taken with the nucleus centered on the PC chip (Malkan et al. 1998). The image being a single exposure with many cosmic-ray events, we cleaned it using the IRAF script *glacos.cl* kindly provided by Dr. Pieter van Dokkum. This script is similar to the script *lacos\_im.cl*

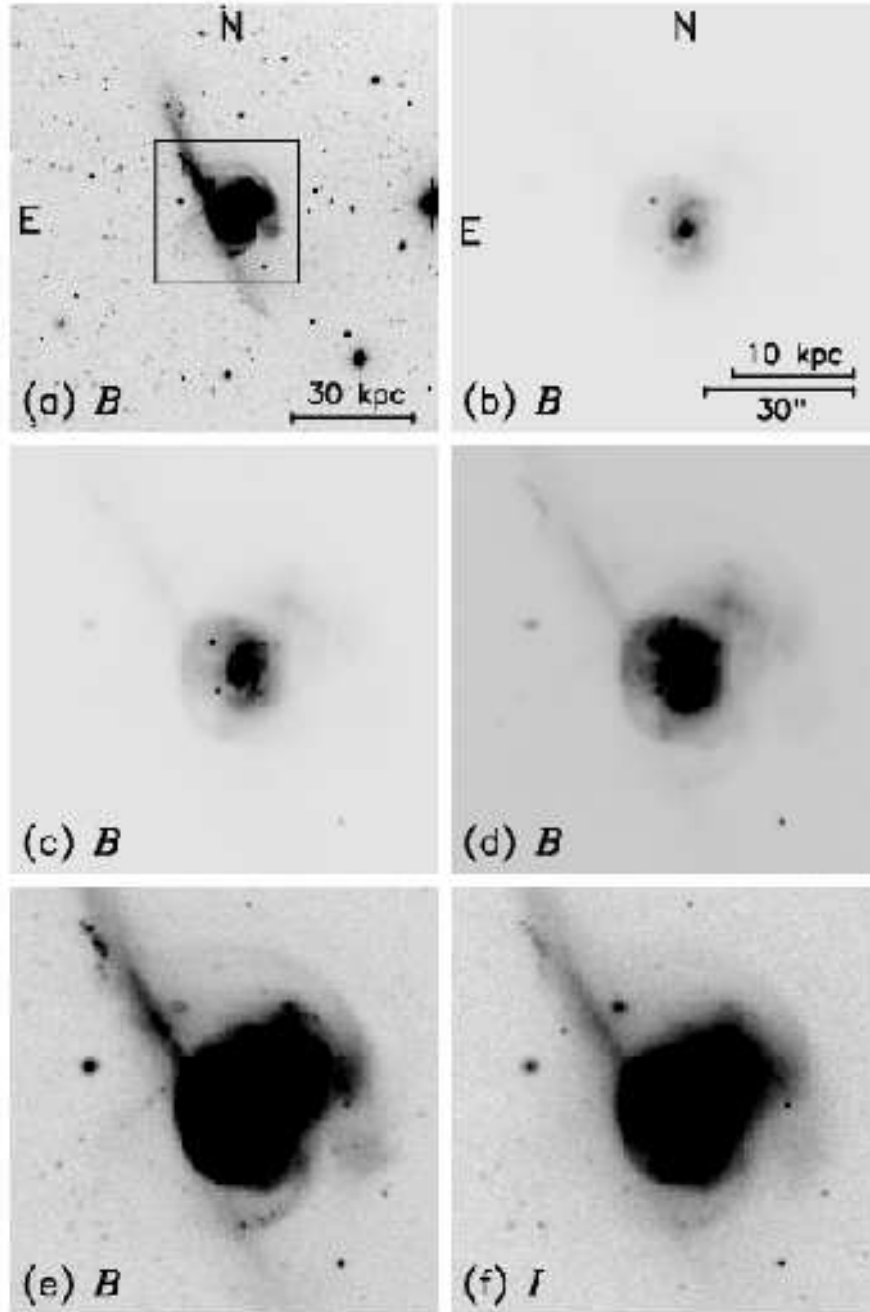


FIG. 1.— Groundbased  $B$  and  $I$  images of NGC 34 obtained with the du Pont 2.5-m telescope. (a) High-contrast display of  $B$  image, showing  $4\frac{1}{3} \times 4\frac{1}{3}$  field of view; the box marks the  $86'' \times 86''$  field of view of the other five panels. Notice the two tidal tails emerging from the system in opposite directions. (b) to (e) Displays of  $B$  image at four different contrasts, enlarged  $3\times$  relative to Panel a. Notice bright nucleus, central disk with spiral structure and dust lanes, two bright star clusters E of nucleus, and faint disk-like material NW of main body. (f) High-contrast display of  $I$  image, for comparison with similar display of  $B$  image in Panel e.

described in van Dokkum (2001), but handles the four frames of a *HST*/WFPC2 image (GEIS-format) in a single operation.

Figure 2 shows (at two different contrasts) a portion of the WFPC2 mosaic image covering the main body of NGC 34 and the bright inner part of the N tail, while Fig. 3 shows (also at two different contrasts) an enlargement of the central regions as imaged on the PC. Note the spiral-shaped dust lanes and the many bright point-like sources that are candidate young star clusters. Photometry and spectroscopy of these candidate star clusters is presented in §§ 2.3 and 2.4 below.

## 2.2. Aperture and Surface Photometry of NGC 34

Figure 4 displays a calibrated blue isophotal map of NGC 34. As this and more detailed maps suggest, the isophotes are roughly concentric around the nucleus out to a surface brightness of  $\mu_B \approx 21.5$  mag arcsec $^{-2}$ , but then bulge toward the NW and increasingly trace tidal debris and tails. The irregularity of the isophotes, especially in the blue and visual, precludes any detailed analysis of the surface-brightness distribution in terms of elliptical isophotes. Hence, we perform photometry only in concentric apertures and then derive *mean* surface-brightness and color-index profiles from it.

Table 2 presents  $V$  magnitudes and  $B-V$ ,  $V-I$  color indices measured in 10 apertures of  $5''$  to  $150''$  diameter centered on

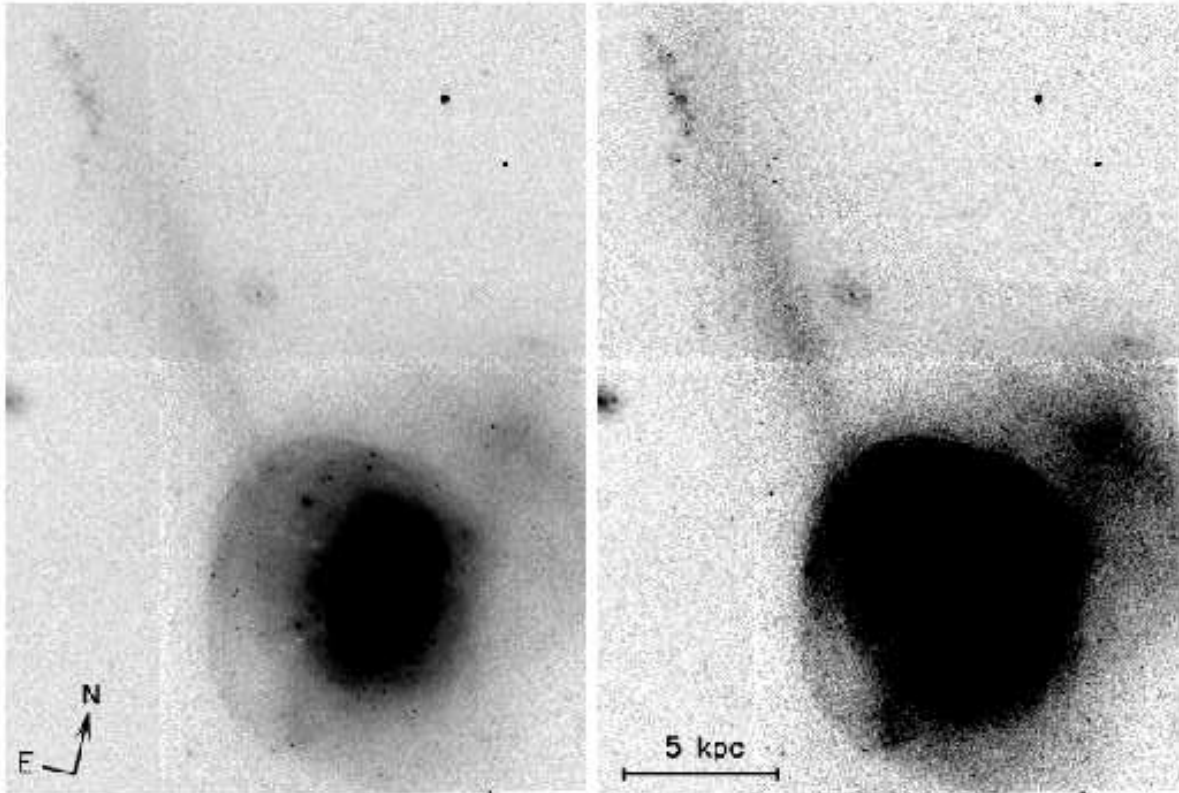


FIG. 2.— Main body and inner part of N tail of NGC 34 as imaged with WFPC2 in V (filter F606W, exposure of 500 s) and displayed at moderate and high contrasts. The part of the mosaicked V image shown measures  $45''8 \times 62''8$  ( $\approx 19 \times 26$  kpc), and the North arrow is  $5''$  long. Notice the sharp ripples to the N, NE, and E of the main body, and the knotty group of young star clusters in the N tail at  $\sim 19$  kpc projected distance from the center.

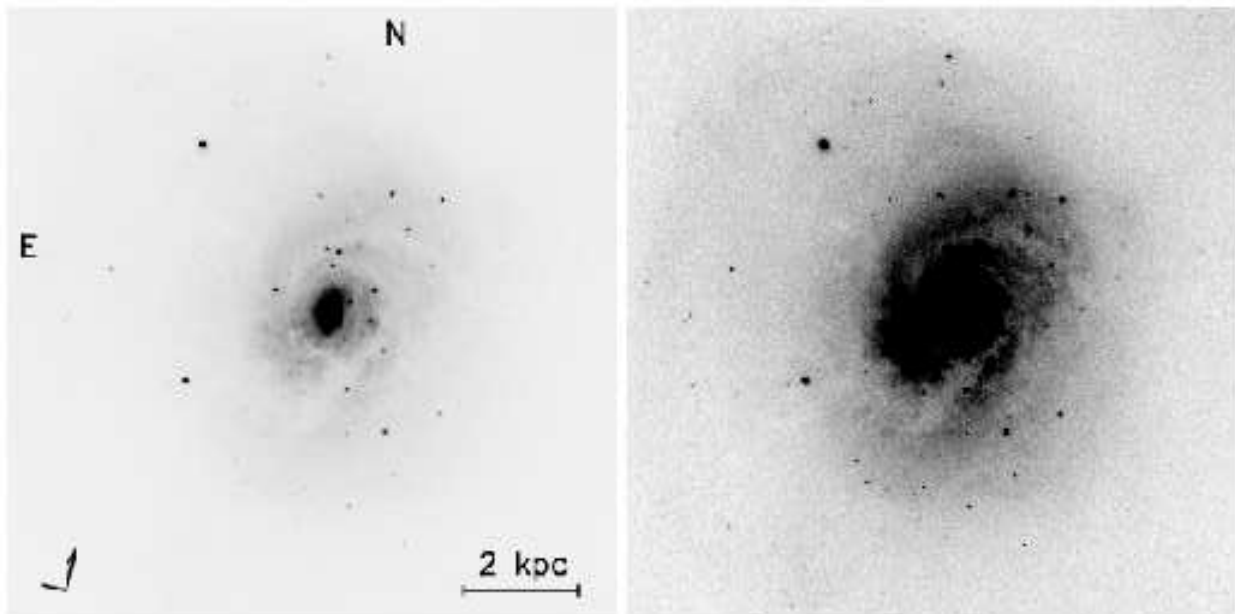


FIG. 3.— Central region of NGC 34 as imaged with the Planetary Camera of WFPC2 in V (filter F606W, exposure of 500 s), displayed at two different contrasts. The field shown measures  $25''5 \times 25''5$  ( $= 10.5 \times 10.5$  kpc) and is centered slightly ESE of the nucleus. The arrow to the lower left measures  $2''$  and points North, while the  $1''$  leg points East. Notice the many point-like sources, which are candidate star clusters, and the intricate, spirally system of central dust lanes.

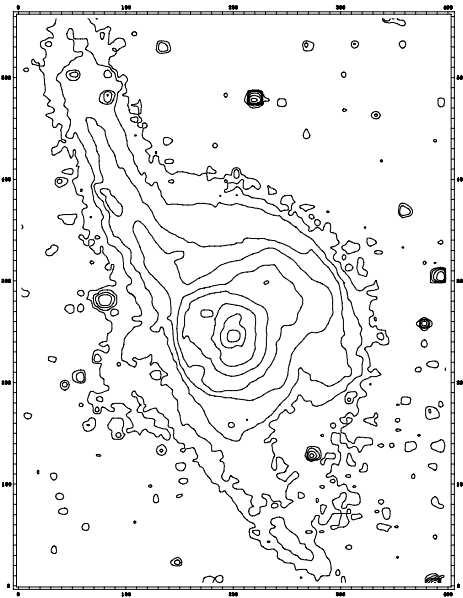


FIG. 4.— Isophotal map of NGC 34, produced from  $B$ -image obtained with du Pont CCD camera. The faintest isophote corresponds to  $\mu_B = 26.5$  mag arcsec $^{-2}$ , and subsequent isophotes increase in surface brightness by 1 mag. To diminish noise, the image has been smoothed with a 5-pix ( $1''.3$ ) square boxcar. North is up, and East to the left. The field of view measures  $104''.3 \times 146''.0$  ( $\approx 43 \times 60$  kpc).

the nucleus. These magnitudes and color indices were extracted from the CCD images of NGC 34 obtained with the du Pont telescope and were calibrated via measurements of 327 Stetson (2000) standard stars in the fields L98 and L110 (Landolt 1973, 1992) observed during the same night. The quoted  $1\sigma$  errors reflect uncertainties in the mean sky levels, which amount to  $\pm 0.14\%$  in  $B$ ,  $\pm 0.18\%$  in  $V$ , and  $\pm 0.08\%$  in  $I$ . The measured magnitudes and colors are used in § 3.3 to derive global photometric parameters for NGC 34.

To derive the mean surface brightness in  $V$  and the mean color indices as functions of radius we performed photometry in many concentric apertures (41 apertures for the ground-based  $BVI$  images and 48 apertures for the  $HST$   $V$  image), using the differences in flux measured in successive apertures. This simple method gives a rough preview of the mean light distribution that the merger remnant is likely to develop as perturbations caused by the merger average out in phase.

Table 3 presents a partial, but representative listing of our measurements at selected radii. Successive columns give the median-area radius  $r$  of the selected ring zone, the fourth root  $r^{1/4}$  and logarithm of this radius, the mean surface brightness  $\mu_V$  measured in  $V$  from the  $HST$  Planetary Camera (PC, part of WFPC2) image ( $\mu_{V,HST}$ ) and from the du Pont image ( $\mu_{V,LCO}$ ), and the mean color indices  $B-V$  and  $V-I$ . The  $\mu_{V,HST}$  surface brightnesses are based on the calibrations and color transformations given by Voit (1998) and Holtzman et al. (1995), with a mean value of  $V-I = 1.10$  from the Las Campanas photometry adopted for the color terms. The  $\mu_{V,LCO}$  surface brightnesses and color indices are calibrated in the same manner as described above for Table 2. When one excludes the central two groundbased measurements at  $r < 0''.5$ , which clearly suffer from seeing effects, the agreement between  $\mu_{V,HST}$  and  $\mu_{V,LCO}$  is reasonably good, with a mean systematic difference of  $\langle \mu_{V,HST} - \mu_{V,LCO} \rangle = +0.05$  mag and rms scatter of  $\pm 0.04$  mag over the radius range  $0''.7-6''.5$ .

The combined surface-brightness and color-index profiles are shown in Fig. 6 and discussed in § 3.2.

### 2.3. Cluster Photometry

NGC 34 hosts a relatively rich system of point-like sources that are candidate young star clusters (Fig. 3, also Figs. 1 and 2). To explore the properties of these clusters, we searched the one  $V$  image currently available from the  $HST$  archive for point sources and performed aperture photometry on them. For the brightest two candidate clusters, we also measured color indices from the  $BVI$  images obtained at Las Campanas (Fig. 1). The archival  $HST$ /WFPC2 image being a single, undithered 500 s exposure in  $V$ , both our search for clusters and the subsequent photometry had to be relatively simple. We ignored the few fuzzy associations and candidate clusters in the N tail, imaged on Chip WF3 of WFPC2 (Fig. 2), and restricted our search to the PC image, which appears to contain all other point sources likely to be associated with NGC 34 (Fig. 3).

To select a complete sample of candidate clusters on the PC image, we used a simplified version of the search algorithm described by Whitmore et al. (2002). The simplified algorithm first invokes the task *daofind* of the IRAF/DAOPHOT package (Stetson 1987) to identify all potential sources  $> 3\sigma$  above background and then filters the resulting source list via various object-shape and photometric parameters. In a final step, the algorithm performs photometry in apertures of 0.5 and 3 pixel radius and selects candidate clusters by requiring a  $\geq 5\sigma$  detection in the larger of the two apertures and a concentration index, defined as the difference between the magnitudes measured in the two apertures, of  $\Delta V_{0.5-3} > 1.5$  mag. This choice of  $\Delta V_{0.5-3}$  filters out hot pixels and noise spikes (see Miller et al. 1997 for an example and more details). We checked by visual inspection that the algorithm found nearly all objects that we would have classified as likely cluster candidates, but rejected hot pixels as well as parts of cosmic-ray events that survived the original cosmic-ray cleaning of the image (§ 2.1). The adopted search algorithm yielded a total of 117 candidate clusters on the PC image, of which 98 have apparent magnitudes  $19.4 \lesssim V < 25.0$  and the faintest has  $V = 25.42$ .

Figure 5 shows a median-masked<sup>3</sup> version of the PC image with all 117 candidate clusters marked, mostly by circles. The 20 brightest candidate clusters, with apparent visual magnitudes in the range  $19.4 \lesssim V \lesssim 22.3$ , are marked by squares with identification numbers. Table 4 gives their coordinates, projected distance from the nucleus of NGC 34, approximate apparent magnitude  $V$  on the Johnson passband system, the corresponding absolute magnitude  $M_V$  corrected for Milky-Way foreground extinction, and the measured concentration index  $\Delta V_{0.5-3}$ . For the two most luminous clusters, reddening-corrected color indices  $(B-V)_0$  and  $(V-I)_0$  measured from the Las Campanas  $BVI$  images are given in the footnotes.

Note that the apparent magnitudes  $V$  on the Johnson system are only approximate because we had to compute them from the magnitudes measured on the instrumental  $V_{606}$  system of WFPC2 without detailed knowledge of the colors for most clusters. We solved the task by assuming that most candidate clusters have the same color as the weighted mean apparent  $V-I$  of the two brightest clusters measured from the Las Campanas images,  $\langle V-I \rangle_{1,2} = 0.67$ , and using the transforma-

<sup>3</sup> See Mighell & Rich (1995, Appendix A) for a description of the masking algorithm, which uses a “low-pass difference filter.”

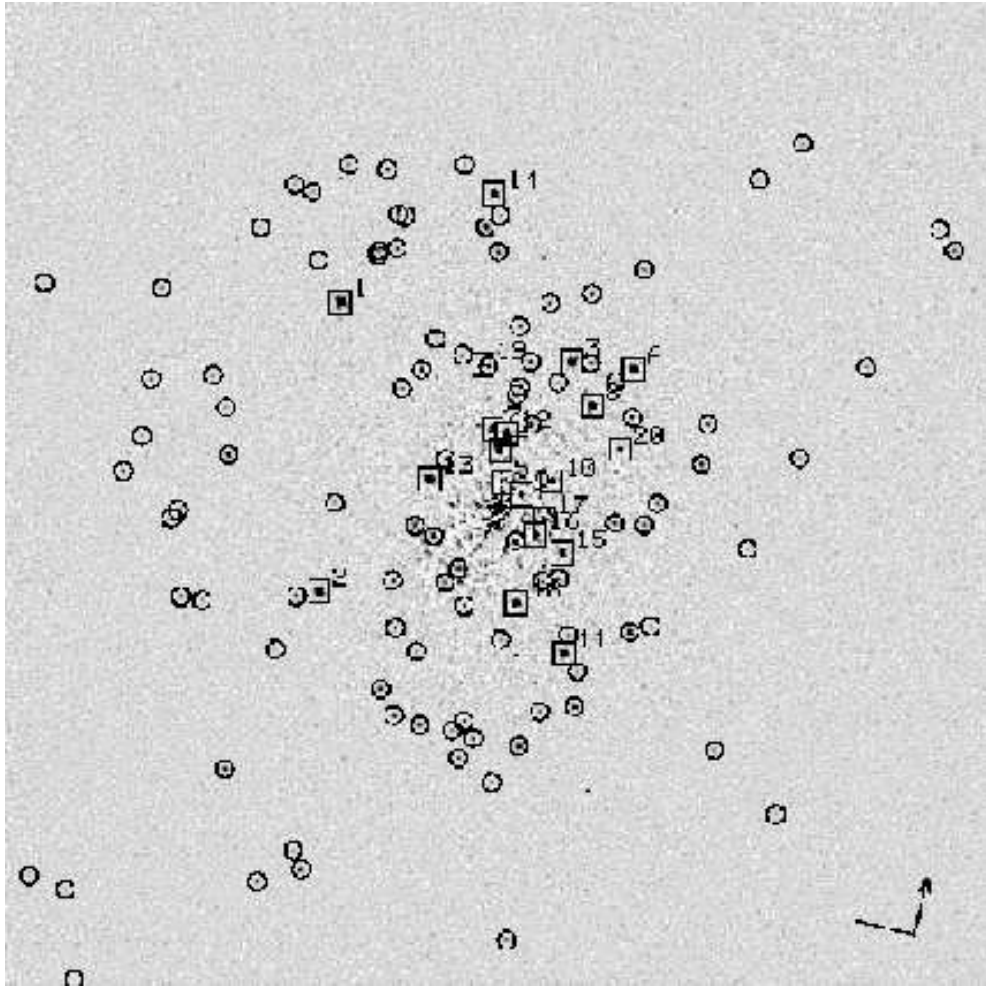


FIG. 5.— Median-masked *HST*/WFPC2 image of NGC 34 in *V* showing 117 candidate clusters, marked mostly by circles. The 20 brightest clusters are marked by squares and ID numbers, with positions and magnitudes given in Table 4. The field of view is that of the Planetary Camera ( $34'' \times 34''$ ), and the arrow pointing north and bar pointing east each measure  $2''$ .

tion equation between the F606W passband and the Johnson *V* band derived by Holtzman et al. (1995, eq. (9) and Table 10). If some clusters were to have  $V-I$  colors deviating by as much as  $\pm 0.5$  mag from the adopted value, their Johnson *V* magnitudes would differ by about  $\pm 0.13$  mag from the values given in Table 4. The photometric standard deviations  $\sigma_V$  listed there do not reflect this transformation uncertainty.

The luminosity function of the cluster system is illustrated and discussed in § 3.5.2.

#### 2.4. Spectroscopy

Spectra of the nucleus and of five candidate star clusters in NGC 34 were obtained with the Low-Dispersion Survey Spectrograph (LDSS-2; Allington-Smith et al. 1994) on the Baade 6.5-m telescope during two observing runs in late summer and fall of 2002 (see Table 1). All spectra were meant to be exploratory and have, therefore, relatively low signal-to-noise ratios, except for the nuclear spectrum.

The five targeted clusters are objects 1, 2, 3, 7, and 13 of Table 4. During the observations, the spectrograph slit of  $1.''03 \times 330''$  was positioned across pairs of bright clusters, yielding spectra of two additional faint clusters in one case (Table 1). The seeing was in the range  $0.''7-0.''9$  (FWHM) throughout the observations. The spectrograph was equipped with a  $600 \text{ g mm}^{-1}$  grism blazed at  $5000 \text{ \AA}$  and a SITE  $2\text{K} \times 2\text{K}$  chip as detector. This combination provided a recip-

rocal dispersion of  $2.41 \text{ \AA pixel}^{-1}$  at  $\lambda 5000 \text{ \AA}$ , a spectral resolution of  $\sim 5.3 \text{ \AA}$ , and a wavelength coverage of about  $3700-6850 \text{ \AA}$ . The scale perpendicular to the dispersion was  $0.''380 \text{ pixel}^{-1}$ .

All reductions were performed with IRAF<sup>4</sup> and its spectral-extraction tasks. First the data frames were debiased, flat-fielded, cleaned of cosmic-ray defects, and wavelength calibrated. Then the spectra of individual clusters were traced on each frame and extracted in  $\sim 2.''1$  ( $= 5.5 \text{ pixel}$ ) wide bands with simultaneous subtraction of sky and galaxy background. For the nuclear spectrum, the extraction band was  $2.''00$  wide, and only sky was subtracted. Next, each spectrum was corrected for atmospheric extinction and flux calibrated via observed standard stars from the list by Hamuy et al. (1992). Each spectrum was then corrected for Earth's orbital motion to heliocentric, and all spectra for any given object were coadded into one sum spectrum per object.

Figure 9 in § 3.4 shows the resulting flux-calibrated spectrum of the strongly reddened nucleus, while Fig. 13 in § 3.5.4 shows the spectra of the two brightest clusters, all plotted versus rest wavelength. In the spectra of the two clusters, note

<sup>4</sup> The Image Reduction and Analysis Facility (IRAF) is distributed by the National Optical Astronomy Observatories (NOAO), which are operated by the Association of Universities for Research in Astronomy (AURA), Inc., under a cooperative agreement with the National Science Foundation.

the strong Balmer absorption lines indicative of A-type main-sequence stars; on expanded plots, these lines are visible up to H12. The spectra of the remaining three clusters are of lower quality and were used only to determine radial velocities (§ 3.5.3).

### 3. RESULTS

#### 3.1. Morphology of NGC 34

The morphology of NGC 34 is complex (Figs. 1 and 2), especially at levels of surface brightness fainter than  $\mu_V \approx 21$  mag arcsec<sup>-2</sup> ( $\mu_B \approx 21.5$ ), where tidal debris increasingly dominate. Above this limit, the central part of the galaxy appears dominated by a bluish disk with some spiral structure, and a very bright nucleus. The following morphological description proceeds from this nucleus outwards.

In the *V*-image obtained with *HST*/WFPC2, the nucleus appears centered at  $\alpha_{J2000} = 00^{\text{h}}11^{\text{m}}06^{\text{s}}.536$ ,  $\delta_{J2000} = -12^{\circ}06'27''.42$ , which is the position of reference we adopt. It agrees to within  $1''.1$  with the astrometric position measured by Argyle & Eldridge (1990) from blue photographic plates obtained at Herstmonceux. The difference is well within the combined errors of this earlier astrometry ( $\sim 0''.3$ ) and of *HST*/WFPC2 positions ( $\lesssim 1''.5$ ). Given the extinction caused by the strong central dust lanes and the deleterious effects of seeing, it is not clear that the groundbased position in the blue is superior to the approximate space-based position in the visual, which is why we adopt the latter.

In the visual, the bright nucleus shows structure on all scales down to the resolution limit of the *HST*/PC. A dust lane at  $r \approx 0''.10$  (41 pc) to the NW of the semi-stellar nucleus seems to either flank this nucleus or perhaps interrupt a small nuclear bulge of semi-major axis  $a \approx 0''.15$  (62 pc) slightly elongated in the same direction (P.A.  $\approx 318^\circ$ ). Surrounding this nucleus or nuclear bulge is a small high-surface-brightness disk of semi-major axis  $a \approx 0''.80$  (330 pc) oriented nearly exactly north–south (P.A. =  $4^\circ$ ). This central disk can be seen as the black-saturated area in the left panel of Fig. 3.

The main disk with spiral structure extends out to  $a \approx 8''$  (3.3 kpc), has an apparent axial ratio of  $b/a \approx 0.72$  (corresponding to an inclination of  $i \approx 44^\circ$  for an infinitesimally thin disk), and has its apparent major axis oriented at P.A.  $\approx 351^\circ$ . Note that the first increasing and then decreasing position angles of the various nested structures (nuclear bulge, small central disk, and main disk) may reflect the presence of a warp. Although there appear to be two relatively smooth main spiral arms, the spiral structure of the disk seems defined mostly by an extensive system of dust lanes rather than by excess luminous matter. The two strongest dust lanes define the inner edges of the two spiral arms, with the southern lane especially broad and prominent.

The entire main disk appears peppered with bright point-like sources, most of which are likely star clusters. Visual inspection offers few clues as to whether these candidate clusters belong to a disk population or a bulge/halo population. A few of them seem to be associated with dust lanes or patches, while the two most luminous clusters (for which we have spectra, § 3.5.4) appear to lie outside the main disk.

Beyond this main disk there is a bewildering variety of structures, including an envelope that contains many sharp-edged ripples and dust lanes, a cloud of luminous debris to the NW, fans and jets of luminous matter, and the two main tidal tails.

Among the envelope’s various ripples are four major ones that we shall designate  $R_1$  to  $R_4$ :  $R_1$  represents the sharp drop-off in surface brightness marking the NNW end of the main disk at  $r \approx 7''.7$  (3.2 kpc);  $R_2$  the next-out, fainter ripple at  $r \approx 10''.9$  (4.5 kpc) NNE (with candidate Cluster 14 superposed on it to the north and Cluster 1 just inside it);  $R_3$  the giant arc-like ripple curving from north through  $r \approx 13''.5$  (5.6 kpc) NE all the way to the south, which forms the envelope’s eastern boundary; and  $R_4$  the faint, more fuzzy and knotty ripple at  $r \approx 23''$  (9.5 kpc) SSW (Figs. 1e and 1f). Note that long sections of  $R_2$  and  $R_3$  appear surprisingly sharp ( $\lesssim 0''.2$ ) even on the *HST*/PC *V*-image (Fig. 2).

The cloud of luminous debris to the NW, which we shall call the “NW Cloud” for short, reaches its diffuse brightness peak at a projected  $r \approx 15''.8$  (6.5 kpc) NNW of the nucleus (Fig. 1d). This cloud itself features much interesting structure (Figs. 1d–1f) and may consist of remnant material from the smaller of the two recently merged galaxies (§ 4.1). Besides several inner looping structures of  $\sim 4''$ – $6''$  diameter seen especially well on the du Pont *B*-image (but not visible in Fig. 1), the NW Cloud features an anvil-shaped extension about  $13''.8$  (5.7 kpc) to the WSW, from which emerges a  $\gtrsim 70''$  (29 kpc) long, curved structure (tidal tail?) to the north and then bends eastward. This anvil-shaped extension shows best in Fig. 1e. Sitting about  $15''$  (6 kpc) SSW of it is an extended cloud of faint debris ( $\mu_B \approx 24$ – $25.5$  mag arcsec<sup>-2</sup>) that appears to connect to both the anvil and the curved structure emerging from it.

The southern part of the NW Cloud appears strongly extinguished by a major aggregate of semi-continuous dust patches ( $\Delta\alpha \times \Delta\delta \approx 6''.5 \times 16'' \approx 2.7 \times 6.6$  kpc), which suggests that the NW Cloud itself may lie *behind* a veil of dust and gas perhaps more associated with the main body of NGC 34.

Besides the two main tidal tails and the long curved structure emerging from the NW Cloud, there are at least two other interesting fans or jets of luminous matter. One is the relatively bright, roughly triangular-shaped protrusion emerging from the region of the main disk to the SSE and best seen in Fig. 1d. This protrusion resembles a bent ribbon of material whose western leg *may* be connected with a weak dust lane seen in absorption against the southern-most part of the main disk. If so, the western leg might lie in front of the main body of NGC 34, and the ribbon itself might loop behind this body on its eastern leg.

The other interesting fan or jet appears to protrude eastward from near the base of the northern tail and extends  $\gtrsim 20''$  (8.4 kpc) ESE from the limit of NGC 34’s envelope defined by Ripple  $R_3$  (Fig. 1a). In its brighter inner part, this feature seems to contain two slightly fuzzy objects that could conceivably be background galaxies, although that would seem rather fortuitous. This luminous “jet” *may* be an extension of very faint material seen north of Ripple  $R_3$ , but it is definitely not an extension of  $R_3$  itself. It can also be traced in Fig. 4 in the form of “appendices” to the  $\mu_B = 23.5$ ,  $24.5$ , and  $25.5$  mag arcsec<sup>-2</sup> isophotes.

Perhaps of greatest value for future model simulations of NGC 34 are the two main tidal tails, of which the N tail is clearly both the brighter and the longer one. It can be traced to a projected distance of at least  $r_{\text{max}} = 92''$  (38 kpc) from the nucleus, while the fainter S tail is optically traceable only out to  $r_{\text{max}} \approx 63''$  (26 kpc).

The N tail features a bright, remarkably straight inner part ending in a group of 5–6 blue knots, the most distant of which lies at a projected distance of  $52''$  (21.5 kpc) from the nu-



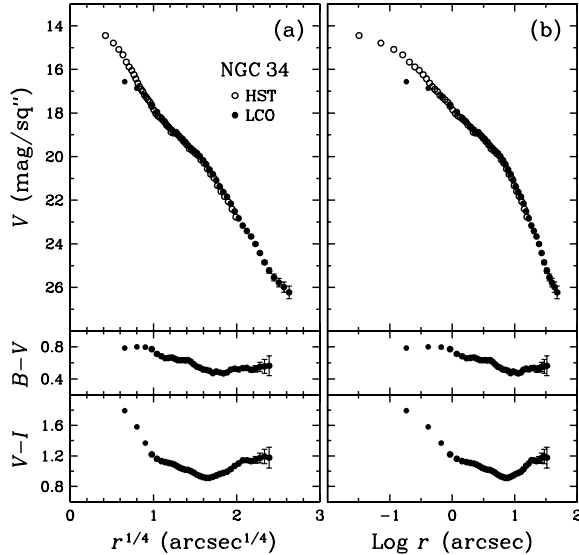


FIG. 6.— Mean radial surface-brightness and color-index profiles of NGC 34 plotted (a) vs fourth root of radius,  $r^{1/4}$ , and (b) vs  $\log r$ . Top panels show mean surface-brightness in  $V$  measured with *HST/PC* and from Las Campanas (“LCO”), while middle and bottom panels show color indices  $B-V$  and  $V-I$ , respectively, measured from Las Campanas; points most affected by seeing (LCO,  $r < 0''.8$ ) are marked by smaller dots. Note the extended “bump” in the  $V$  vs  $r^{1/4}$  profile centered on  $r^{1/4} \approx 1.65$  ( $r \approx 7''.4 \approx 3.0$  kpc), representing extra light from the blue main disk. The sharp “knee” in the  $V$  vs  $\log r$  profile at  $\log r \approx 0.87$  is caused by the same disk. For details, see § 3.2.

cleus. On the *HST/WFPC2*  $V$ -mosaic image, these knots resolve into a number of relatively point-like sources (likely star clusters) and more extended, unresolved stellar associations (Fig. 2). The fact that the inner half of the tail appears straight and narrow suggests that it consists of former disk material seen nearly edge-on. Further out, the N tail becomes slightly curved and more fan-like, suggesting that westwardly this former disk material may warp.

Following the brighter part of the N tail inward one can see a dust lane in absorption against the luminous background of Ripple  $R_3$ , from where it passes south of Cluster 1 and apparently ends in a major dust patch at  $r = 5''.8$  (2.4 kpc) from the nucleus (P.A. =  $66^\circ$ ). Thus, the N tail clearly crosses *in front* of the main body of NGC 34. It would be of interest to know whether and how this tail connects further inward or to the east. This cannot be established unambiguously from the present images. *If* some roughly parallel dust lanes seen further south of the above dust patch also belong to this tail, then the tail may connect to the very prominent dust lane spiraling toward the nucleus on the inside of the southern spiral arm (Fig. 3).

The S tail appears much less well defined than the N tail, being both fainter and more diffuse. It is well visible beyond Ripple  $R_4$ , but difficult to trace further in. On its way in, its western edge seems to either hug, or coincide with, the eastern leg of the triangular-shaped luminous protrusion described above, and the whole tail “fades” into a low-surface-brightness, SE area of the envelope which may, or may not, be obscured by extinction. If it were to be extinction and dust in the S tail causes it, then the S tail would enter the main body from the front, like the N tail. This is an unexpected, and perhaps impossible, geometry. Unfortunately, the signal-to-noise ratio of the *HST/PC*  $V$ -image in this region is too low to settle the issue of possible dust extinction morphologically. To do so, deeper high-resolution images (e.g., with *HST/ACS*) in

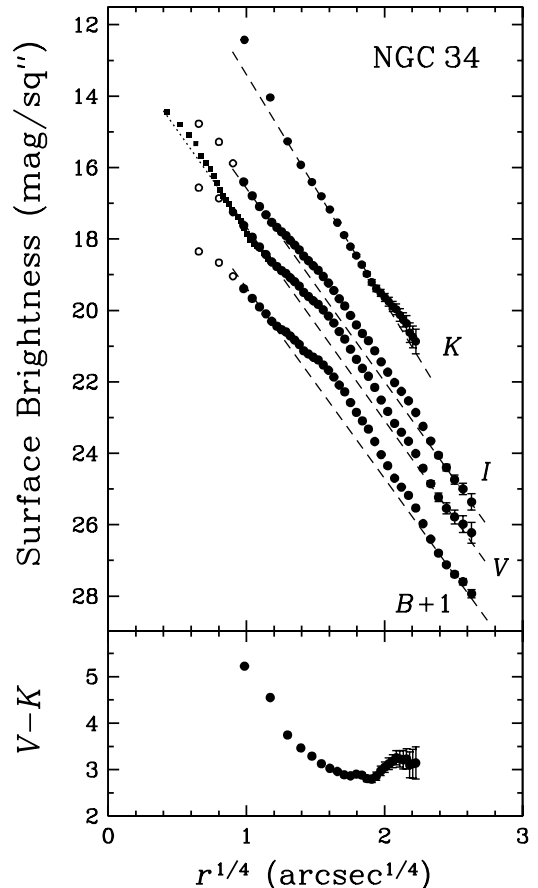


FIG. 7.— Mean radial profiles of (top) surface brightness in  $BVIK$  and (bottom) color index  $V-K$  plotted vs fourth root of radius,  $r^{1/4}$ . The  $K$  data are from Rothberg & Joseph (2004), while the  $BVI$  data are from Las Campanas (filled and open circles) and the *HST/PC* (small squares). The  $B$  profile is shown shifted by +1 mag for clarity. The dashed lines represent least-squares fits (in  $K$ ) or lines drawn parallel to such fits (in  $BVI$ ); see text for details. Note that the slope of the  $K$ -profile is significantly steeper than the slopes of the  $B$ -,  $V$ -, and  $I$ -profiles, leading to the strong inner color gradient seen in  $V-K$ .

two or three passbands will be needed.

### 3.2. Surface-Brightness Distribution

Figure 6 shows the mean radial profiles of  $V$  surface brightness and  $B-V$  and  $V-I$  color (§ 2.2) in NGC 34, plotted both vs the fourth root of radius,  $r^{1/4}$ , and vs  $\log r$ . These various profiles show two related salient features.

First, although overall the  $V$  profile appears to approximate an  $r^{1/4}$  law (de Vaucouleurs 1953) reasonably well, the deviations of the data points in Fig. 6a from a straight line are highly significant (most error bars being smaller than the size of the data points). The main feature is an extended “bump” in the  $V$  vs  $r^{1/4}$  profile, centered on  $r^{1/4} \approx 1.65$  ( $r \approx 7''.4 \approx 3.0$  kpc) and showing up in the  $V$  vs  $\log r$  profile as a relatively sharp “knee” or break in the slope at  $\log r \approx 0.87$ . Note that the bump and knee are seen clearly in both the ground-based and the *HST* data (filled and open circles, respectively), whence they represent a real feature.

And second, the color-index profiles display minima in both  $B-V$  and  $V-I$  near the radii of the bump and knee ( $\sim 3-4$  kpc), indicating that the extra light causing these features in the  $V$  profile must be quite blue.

Comparisons with simple model light distributions that



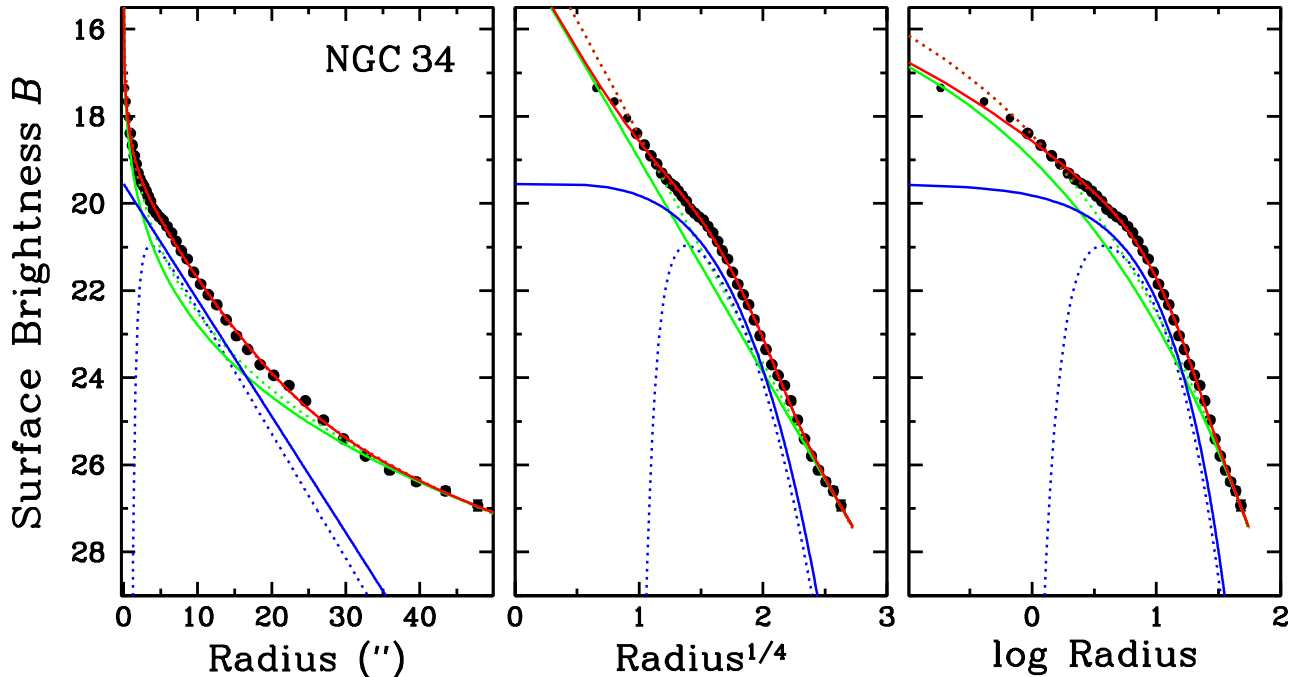


FIG. 8.— Sph + eD model fits to  $B$  profiles plotted vs (left) radius  $r$ , (middle)  $r^{1/4}$ , and (right)  $\log r$ . Data points represent  $B$ -profile measured from Las Campanas, while the solid lines mark the best Sph + eD fit (red) and its component spheroid (green) and disk (blue) for the case of an exponential disk without central hole. Dotted lines mark the corresponding best fits for an exponential disk with a central hole. Note how the exponential disk produces the “bump” in the  $r^{1/4}$  profile and the “knee” in the  $\log r$  profile.

contain contributions from both an  $r^{1/4}$ -law spheroid and an exponential disk show that similar bumps and knees trace relatively bright exponential disks. Hence, the above two features in NGC 34 suggest the presence of a significant, blue exponential disk embedded in a redder spheroid. This blue disk presumably corresponds to the “main disk with spiral structure” noted morphologically as extending out to  $a \approx 3.3$  kpc (§ 3.1).

As a first test of this hypothesis, Fig. 7 displays the individual surface-brightness profiles in  $B$ ,  $V$ , and  $I$  plotted vs  $r^{1/4}$ , and for comparison also the mean surface-brightness profile in  $K$  similarly measured by Rothberg & Joseph (2004). To help assess the amplitudes of the bump in  $BVI$ , straight dashed lines with slopes equal to least-squares fits to all the data not seriously affected by seeing (filled circles) have been drawn with small vertical shifts so as to roughly form lower boundaries to the observed profiles. Note that the relative amount of light in the bump increases significantly from  $I$  through  $V$  to  $B$ , while no similar bump is observed in  $K$  (where the fit is taken from Rothberg & Joseph). Hence, this increasing amplitude with decreasing wavelength indeed supports the view that the hypothetical disk is significantly bluer than the host spheroid, suggesting a population of young disk stars.

A second, more thorough test of the above hypothesis is to fit the observed surface-brightness profiles with models consisting of an  $r^{1/4}$ -law spheroid plus an exponential disk (e.g., Kormendy 1977; Baggett et al. 1998) and to see (1) how much such fits improve the mean residuals over fits with a pure  $r^{1/4}$  law and (2) how consistent the model parameters obtained independently from  $B$ ,  $V$ , and  $I$  are. Using the IRAF/STSDAS task *nfit1d*, we performed such “Sph + eD” (spheroid plus exponential disk) model fits in both magnitude-vs-radius and linear-flux-vs-radius space, and with exponential disks with and without central hole. To obtain consistent color infor-

mation we ignored the *HST* data in  $V$  and fitted only the mean  $BVI$  surface-brightness profiles measured from Las Campanas data.

Figure 8 shows how these fits appear when the surface brightness in  $B$  is plotted vs linear radius  $r$ , vs  $r^{1/4}$ , and vs  $\log r$ . Superposed on the observations (data points), the solid lines mark the best Sph + eD fit (red) and its component spheroid (green) and disk (blue) for the case of an exponential disk without central hole. Correspondingly, dotted lines mark the best fit for the case of an exponential disk with a central hole (Kormendy 1977; Baggett et al. 1998). As a comparison of the solid and dotted red lines shows, the Sph + eD model profiles without and with a central hole in the exponential disk fit the data nearly identically well over the fitting range (large data points from  $r = 0''.92$  to  $47''.8$ ), though—not surprisingly—they diverge at  $r \lesssim 1''$ . The model profiles represent the observed  $B$  (and also  $VI$ ) surface brightnesses remarkably well, with rms residuals of only 0.07 mag in  $B$ , thus strongly supporting the hypothesis that the bump in the  $r^{1/4}$ -profile and the knee in the  $\log r$ -profile are caused by the presence of an exponential disk.

Table 5 summarizes both the pure  $r^{1/4}$ -law fits in  $BVI$  mentioned above and the new Sph + eD model fits. As comparisons of the rms residuals in the table and of Figs. 7 and 8 suggest, allowing for the presence of an exponential disk in addition to the spheroid brings a dramatic improvement in the fits, reducing the rms residuals in the various passbands by factors of 2–4. Also, the two scale lengths of the Sph + eD model, the effective radius  $r_{\text{eff}}$  of the spheroid and the scale length  $\alpha$  of the exponential disk, agree remarkably well among the three passbands, as does the “hole radius”  $r_h$  in the case of the exponential disk with a central hole.<sup>5</sup> Thus, the model

<sup>5</sup> We note, however, that the model without a hole in its exponential disk reproduces the total color index  $(V-I)_T$  of NGC 34 slightly better (to within

parameters obtained independently from  $B$ ,  $V$ , and  $I$  are reasonably consistent, which again supports the hypothesis that an approximately exponential disk is present in NGC 34.

What are the relative luminosity and colors of this model disk? If we pick the best-fit Sph+eD model without a hole in the disk, the model disk contributes 51%, 43%, and 27% of the total  $B$ ,  $V$ , and  $I$  light, respectively, within  $r = 15$  kpc (corresponding to about the  $B = 26.5$  isophote, see § 3.3). Its absolute visual magnitude, corrected for Galactic foreground (but not internal) extinction, is  $M_{V,0} = -20.61$ , and its colors are  $(B-V)_{\text{eD},0} = 0.36 \pm 0.02$  and  $(V-I)_{\text{eD},0} = 0.52 \pm 0.02$ . If, on the other hand, we pick the best-fit Sph+eD model *with* a hole in its disk, then the model disk contributes about 34%, 26%, and 18% of the total  $B$ ,  $V$ , and  $I$  light, respectively, and has an absolute luminosity  $M_{V,0} = -20.11$  and color indices  $(B-V)_{\text{eD},0} = 0.28 \pm 0.02$  and  $(V-I)_{\text{eD},0} = 0.59 \pm 0.02$ . Thus, in either case the exponential disk is very blue and contributes significantly to the total optical luminosity of NGC 34.

An alternative way to state this is that the present-day bulge-to-disk ratios of NGC 34 for the model without a central hole in its disk are  $(B/D)_B = 0.94$ ,  $(B/D)_V = 1.32$ , and  $(B/D)_I = 2.7$  (within  $r = 15$  kpc), while those for the model with a central hole are  $(B/D)_B = 1.9$ ,  $(B/D)_V = 2.8$ , and  $(B/D)_I = 4.6$ . These bulge-to-disk ratios will, of course, change as the stellar populations of the bulge and blue disk age.

### 3.3. Systemic Velocity and Absolute Magnitude

The heliocentric systemic velocity, measured from six absorption lines in the spectrum of the nucleus (§ 3.4), is  $c_{\text{Z}_{\text{hel,sys}}} = 5870 \pm 15$  km s<sup>-1</sup>. This value agrees to within  $1.1 \sigma$  (combined error) with the modern optical measurement of  $5821 \pm 44$  km s<sup>-1</sup> by da Costa et al. (1998) and to within  $0.7 \sigma$  with that of  $5881 \pm 2$  km s<sup>-1</sup> (from the Ca II triplet) by Rothberg & Joseph (2006a), but disagrees significantly with many older optical measurements (e.g., de Vaucouleurs et al. 1991) and with the value of  $5931 \pm 11$  km s<sup>-1</sup> until recently adopted in the NASA/IPAC Extragalactic Database (NED).

The likely reason for the disagreement with older optical measurements, which tend to yield 100–150 km s<sup>-1</sup> lower values, is that these measurements often included the strong Na D lines, shown in § 3.4 to yield a velocity about 620 km s<sup>-1</sup> lower than the above systemic velocity due to the presence of a gaseous outflow. The significantly higher systemic velocity until recently given in NED, on the other hand, was based on the mean heliocentric velocity from compiled integrated H I observations (Botinelli et al. 1990).<sup>6</sup> In merging galaxies, the H I distribution is often strongly asymmetric (e.g., Hibbard & van Gorkom 1996), and the mean H I velocity can be a poor measure of the galaxies' or remnant's systemic velocity. Hence, and despite the high intrinsic accuracy of H I velocities, the new optical absorption-line velocity of the nucleus of NGC 34, supported by that measured in the near-infrared from the Ca II triplet by Rothberg & Joseph, is probably more accurate.

After correction to the barycenter of the Local Group via  $\Delta c_{\text{Z}_{\text{LG-hel}}} = 300 \sin l \cos b = +91$  km s<sup>-1</sup> (Sandage & Tammann 1975), the systemic velocity of NGC 34 is  $c_{\text{Z}_{\text{LG}}} = +5961$  km s<sup>-1</sup>, leading to the adopted distance of 85.2 Mpc for  $H_0 = 70$  km s<sup>-1</sup> Mpc<sup>-1</sup> (§ 1).

0.03 mag) than does the model with a central hole (to within 0.05 mag), while both models reproduce the measured  $(B-V)_T$  very well (to  $\lesssim 0.01$  mag).

<sup>6</sup> As of 2006 August, the new value adopted by NED for the heliocentric velocity is that measured by Rothberg & Joseph (2006a).

To calculate the absolute magnitudes of NGC 34 in different passbands, we first need to measure total magnitudes, traditionally defined as integrated magnitudes within the  $\mu_B = 26.5$  mag arcsec<sup>-2</sup> isophote. From the isophotes shown in Fig. 4, and ignoring their extensions along the tidal tails, we determined that the area within the above isophote corresponds to that of a circular aperture of radius  $r = 36''.5$  (15.1 kpc), and we approximated the total magnitudes by interpolating the magnitudes measured in concentric apertures (Table 2) to this radius. The resulting total magnitudes  $B_T$ ,  $V_T$ , and  $I_T$  are given in Table 8 below. For comparison, Table 8 also gives the total  $K$  magnitude measured by Rothberg & Joseph (2004) and here corrected to the same aperture (i.e.,  $\sim \mu_B = 26.5$  isophote) as the total optical magnitudes.

Based on these total apparent magnitudes and the adopted distance and foreground extinction (§ 1), the absolute visual magnitude and foreground-reddening-corrected total color indices of NGC 34 are  $M_V = -21.57$ ,  $(B-V)_{T,0} = 0.55 \pm 0.02$ ,  $(V-I)_{T,0} = 1.05 \pm 0.01$ , and  $(V-K)_{T,0} = 3.15 \pm 0.03$ , respectively.

From the multi-aperture photometry given in Table 2 and the isophotes, we estimate that the extra light *beyond* the above  $r = 36''.5$  aperture used for the total magnitudes is about  $7\% \pm 3\%$  in  $V$  and originates mostly in the two main tidal tails.

### 3.4. The Nuclear Spectrum: Strong Outflow

As described in § 1, the appearance of the nuclear spectrum of NGC 34 has variously been attributed to the presence of a Seyfert 2 nucleus, a nuclear starburst, or a combination of both.

The new nuclear spectrum shown in Fig. 9 does not contribute toward settling this controversy, but does reveal that there are systematic velocity differences between the ionized gas and the stars, and that some of the cool gas—as traced by Na I D absorption—is experiencing a strong outflow of the kind often observed in IR-luminous galaxies with star formation rates  $\gtrsim 10 M_\odot \text{ yr}^{-1}$  (Rupke et al. 2005; Veilleux et al. 2005).

After we discovered the strong blueshift of the Na D doublet, we determined the systemic *stellar* velocity in two ways: by measuring individually five Balmer lines between H $\gamma$  and H10 plus the Ca II K line and computing the mean velocity, and by cross-correlating the blue part of the nuclear spectrum ( $\lambda\lambda 3820\text{--}5050$ ), clipped of emission lines, with the template spectrum of the massive young cluster NGC 7252:W3 described in § 3.5.3 below. The weighted average of the two methods yielded the adopted heliocentric systemic velocity of  $5870 \pm 15$  km s<sup>-1</sup> (§ 3.3).

Relative to this systemic stellar velocity, the emission lines from ionized gas show small blueshifts with considerable scatter,<sup>7</sup> corresponding to a mean velocity of about  $-75 \pm 23$  km s<sup>-1</sup>. Although this velocity likely indicates an outflow of ionized gas from the nucleus, the evidence is not unambiguous since the mean position of the emitting gas along the line of sight is unknown.

Tracing the line-of-sight velocities of cool, neutral gas between us and the nucleus of NGC 34, the Na I D doublet appears both broad and blueshifted relative to the stars. This can be seen directly in Fig. 10, which compares the line profile of this doublet for the nucleus (solid line) with the profiles for

<sup>7</sup> The blueshift of the H $\beta$  emission line relative to the stellar H $\beta$  absorption line is directly visible in the lower left panel of Fig. 9.

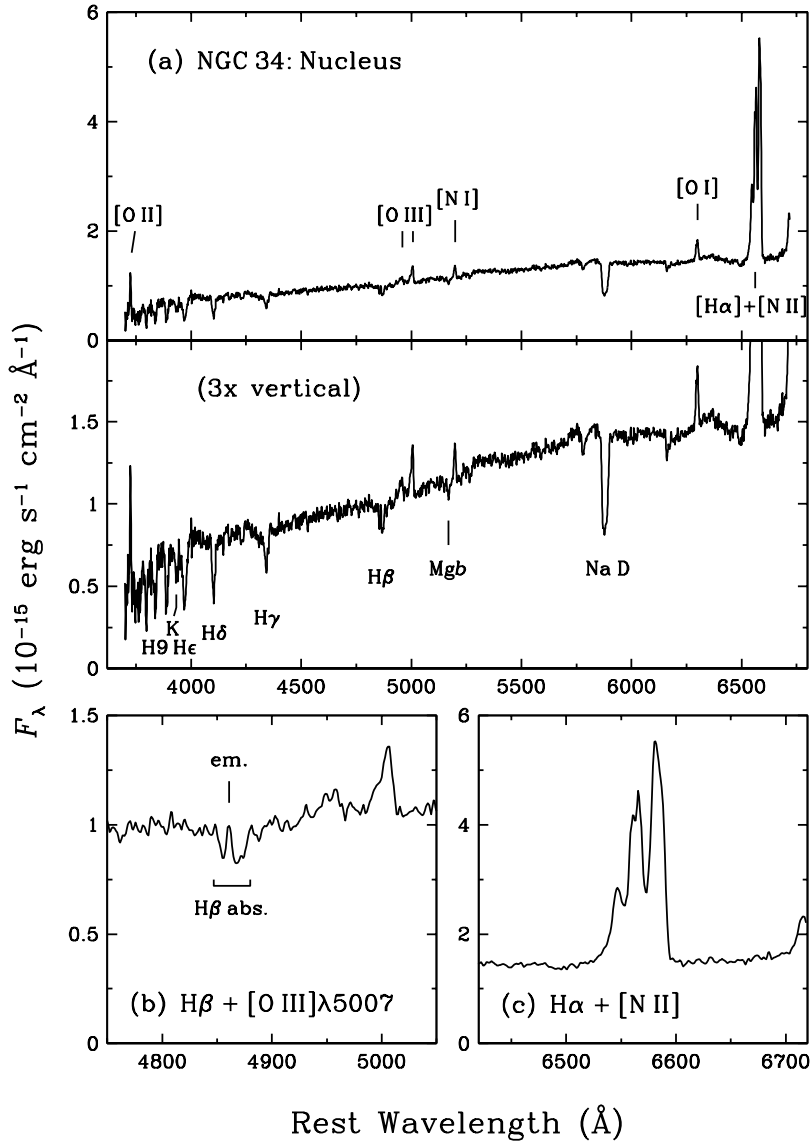


FIG. 9.— (a) Ultraviolet-to-red spectrum of the NGC 34 nucleus, obtained with the Baade 6.5-m telescope and LDSS-2 spectrograph through a  $1''.03 \times 2''.0$  slit aperture oriented at P.A. =  $144.5^\circ$ . The spectrum is flux calibrated and plotted vs. rest wavelength. Emission lines are identified in the upper panel, absorption lines in the lower panel with  $3\times$  expanded flux scale. Panels (b) and (c) show spectral details around  $H\beta$  and  $H\alpha$ , respectively, on a scale  $5\times$  enlarged in wavelength. Note the poststarburst nature of the spectrum in the UV–blue region, the small blue-shift of the  $H\beta$  emission relative to the absorption, the somewhat broadened emission lines, and the very strong Na D absorption, whose measured blueshift indicates an outflow with a mean velocity of about  $-620 \text{ km s}^{-1}$ .

the two luminous clusters 1 and 2, all plotted vs *rest* wavelength. The nuclear line profile is  $\sim 2.3\times$  as wide (FWHM) as the cluster line profiles, and the measured mean position indicates a mean outflow of  $-620 \pm 60 \text{ km s}^{-1}$  from the nucleus. The maximum outflow velocity of the cool gas, estimated from the shift between the blue edges of the nuclear and cluster line profiles at half minimum (arrows in Fig. 10) is about  $-1050 \pm 30 \text{ km s}^{-1}$ . These mean and maximum outflow velocities indicate an outflow that is strong, even for a galaxy with a star formation rate of  $70 \pm 20 M_\odot \text{ yr}^{-1}$  like NGC 34 (§ 4.3).

The spatial extent of this outflow needs to be established before the mass involved in the outflow can be calculated. In principle, spectra of the many young star clusters can be used to map the outflow. However, the spectra presently available for five clusters (§§ 2.4 and 3.5.3) have too low signal-to-noise ratios to lead to conclusive results. Whereas the Na D doublets in clusters 1 and 2 appear to be mostly of stellar origin,

with perhaps a mildly blue-shifted extra component in Cluster 2 (Fig. 10), the doublets of clusters 3 and 7 do seem to indicate major blue shifts relative to both the clusters and the galaxy, even though the spectra are very noisy. Relative to the systemic velocity of NGC 34, the blueshift of the Na D doublet in cluster 3 ( $\sim 2.3 \text{ kpc NNW}$  of the nucleus) appears to be about  $-390 \pm 100 \text{ km s}^{-1}$ , while for cluster 7 ( $1.1 \text{ kpc NNE}$  of nucleus) it appears to be about  $-460 \pm 200 \text{ km s}^{-1}$ . Clearly, new spectra for more clusters are needed to properly map the full outflow.

Note that the shapes of the  $[O \text{ III}] \lambda 5007$  and  $H\alpha + [N \text{ II}] \lambda\lambda 6548, 6583$  emission lines seem to indicate velocity broadening as well, even though the latter three lines blend in part because of the limited,  $\sim 5.3 \text{ \AA}$  resolution of our observations. Yet, much higher-resolution observations made by Busko & Steiner (1990) with a Coudé spectrograph confirm that the  $H\alpha + [N \text{ II}]$  lines are significantly broadened (FWHM =  $264 \pm 7 \text{ km s}^{-1}$  for  $H\alpha$  and  $384 \pm 12 \text{ km s}^{-1}$

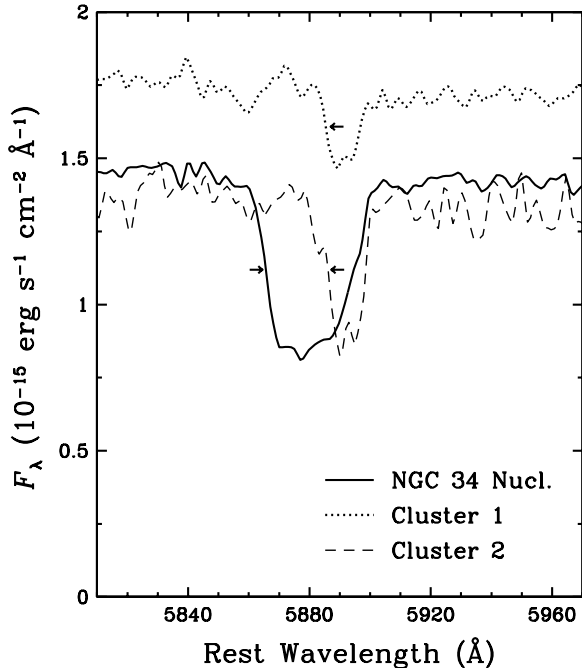


FIG. 10.— Enlarged portions of the nuclear spectrum and of two cluster spectra around the Na I D doublet, plotted vs rest wavelength. The flux scale applies to the nucleus, while each cluster spectrum has been scaled arbitrarily (but with zero level fixed at the bottom). Note the larger width and blueshift of the nuclear doublet, indicating a gaseous outflow with a mean velocity of about  $-620 \text{ km s}^{-1}$  and a maximum velocity of about  $-1050 \text{ km s}^{-1}$ . This maximum velocity has been derived from the shifts between the blue edges of the nuclear gas outflow and of the (mostly) stellar cluster doublets (arrows).

for [N II]  $\lambda 6583$ ) and *may* have weak underlying broader components. Clearly, the apertures used to extract the nuclear spectrum by both Busko & Steiner ( $1''.2 \times 5''.0$ ) and ourselves ( $1''.03 \times 2''.0$ ) cover nuclear areas large enough to comprise varied ionized-gas motions, and new observations with higher *spatial* resolution are needed to better isolate individual narrow- and broad-line components.

Finally, it seems worth pointing out that the optical nuclear spectrum appears not only strongly reddened, but also highly composite (Fig. 9). Blueward of  $\lambda \approx 4500 \text{ \AA}$  the spectrum is dominated by strong Balmer absorption lines typical of a poststarburst population. A comparison of the region containing the Ca II K line and the Balmer lines H8, (H+)H $\epsilon$ , and H $\delta$  with model spectra of simple stellar populations computed by Bruzual & Charlot (2003) suggests a poststarburst age of about 300–400 Myr. Yet, longward of  $\lambda 4500$  the optical spectrum is increasingly dominated by H II-region-like emission lines, suggesting the presence of an *ongoing*, strongly extinguished starburst. Of course, the main evidence for such an obscured central starburst comes from the infrared (see § 1). The combined evidence suggests, then, that the region of strong starburst activity has shrunk with time and is now restricted to a highly obscured central region of  $\lesssim 1 \text{ kpc}$  radius (see *V–K* profile of Fig. 7). Presumably, it is from this central region that the gaseous outflow originates.

### 3.5. The System of Young Massive Clusters

The central system of 117 candidate young massive clusters in NGC 34 (§ 2.3) is conspicuous (Figs. 3 and 5) and contains 17 objects with  $-13.0 \geq M_V \geq -15.4$  (Table 4). The present subsection describes the clusters' spatial distribution, luminosity function, known line-of-sight velocities, and spec-

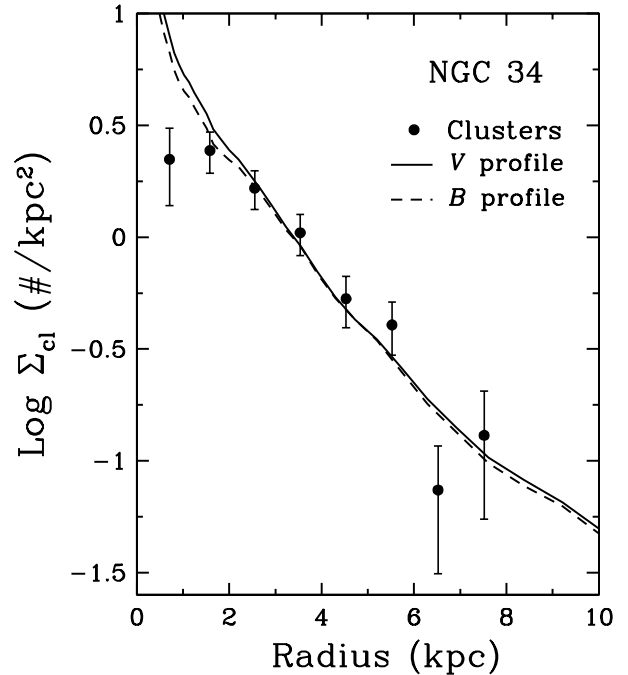


FIG. 11.— Radial distribution of candidate clusters in NGC 34. The surface number density of clusters,  $\Sigma_{\text{cl}}$  (data points with error bars), is compared with the mean surface-brightness profiles in *V* (solid line) and *B* (dashed) of the underlying galaxy. The *V* and *B* profiles have been shifted vertically by arbitrary amounts. Note the good agreement between the centrally concentrated cluster distribution and the underlying galaxy light, except within  $r \lesssim 1.5 \text{ kpc}$  where incomplete cluster detection due to the bright galaxy background becomes significant.

troscopically estimated ages.

#### 3.5.1. Spatial Distribution

Visual inspection of Fig. 5 suggests that the 117 candidate young massive clusters lie strongly concentrated toward the center of NGC 34 and are distributed approximately uniformly in position angle, though with a slight excess in numbers toward the NE and a slight deficiency toward the WSW.

Figure 11 shows the radial distribution of the clusters' projected surface number density,  $\Sigma_{\text{cl}}$ , plotted vs linear radius. This surface density, expressed as a number per  $\text{kpc}^2$ , was determined in successive circular annuli of 1 kpc width centered on the nucleus and has not been corrected for background objects or completeness. Given that even the faintest of the 117 clusters are relatively bright,  $V \approx 25.4$ , the contribution from background objects over the total field of view ( $34'' \times 34''$ ) is negligible, while any completeness correction will mainly affect  $\Sigma_{\text{cl}}$  in the innermost 1–2 kpc, where the galaxy background is brightest. For comparison the figure also shows, with arbitrary vertical shifts, the surface-brightness distribution of the underlying galaxy in *B* and *V*.

The main result is that over most of the range in radius covered,  $r \approx 1.5\text{--}8 \text{ kpc}$ , the surface number density of clusters tracks the underlying galaxy light remarkably well. This is similar to the situation observed in other recent merger remnants (e.g., NGC 3921: Schweizer et al. (1996); NGC 7252: Miller et al. 1997) and seems to indicate that violent relaxation redistributed the general luminous matter of the two merging galaxies in roughly the same manner as it redistributed the giant molecular clouds and young clusters forming from them (Schweizer 2002). If this conclusion is correct, the apparent deficit of clusters within the central  $\sim 1.5 \text{ kpc}$  ra-

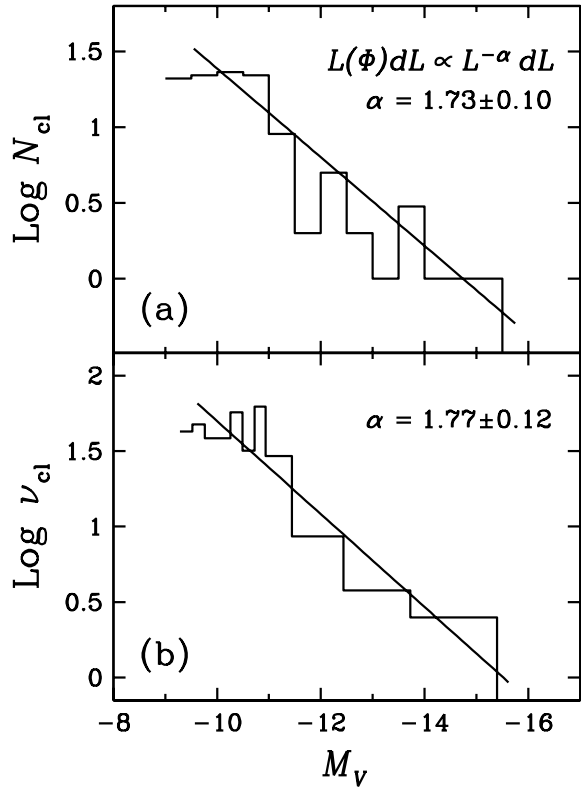


FIG. 12.— Luminosity function of candidate young massive clusters in NGC 34. (a) Logarithm of number of clusters per 0.5-mag bin,  $N_{cl}$ , plotted vs.  $M_V$ . (b) Logarithm of number of clusters per magnitude interval,  $\nu_{cl}$ , derived from constant-number bins of varying widths and plotted vs.  $M_V$ . Straight lines show power laws fit by least squares, with exponent  $\alpha$  marked (for details, see text).

dus relative to the general light distribution is likely due to the growing incompleteness in cluster detection as the brightness of the galaxy background increases.

Assuming that, were it not for this central incompleteness, the surface density  $\Sigma_{cl}$  would track the mean  $V$ -profile of NGC 34 exactly, the number of candidate clusters within  $r \leq 2$  kpc would increase from 30 to about 53, and the total number within the field of view imaged by the PC of WFPC2 ( $r \lesssim 8$  kpc) would increase from 117 to about 140 candidate clusters with  $V \lesssim 25.4$  ( $M_V \lesssim -9.3$ ).

Finally, the effective radius of the candidate-cluster system is  $r_{eff,cl} = 3.1$  kpc without incompleteness correction and  $r_{eff,cl} \approx 2.6$  kpc with the above estimated correction.

### 3.5.2. Luminosity Function

Of the 117 candidate young massive clusters, 87 are more luminous than  $M_V = -10.0$ . The most luminous cluster has  $M_V = -15.36$ , while the faintest candidate cluster detected on the one *HST*/WFPC2 500s exposure has  $M_V = -9.32$ .

The cluster luminosity function (LF) was derived as follows. To minimize effects of incompleteness, which are most severe near the galaxy’s center (§ 3.5.1), we excluded the central 17 clusters with  $r < 1.25$  kpc from the analysis, leaving 100 clusters from which to determine the LF. Then we binned the clusters in bins of 0.5 mag width centered at  $M_V = -9.25, -9.75, \dots, -15.25$ . Figure 12a shows the resulting LF plotted logarithmically versus  $M_V$  (histogram) and—superposed—a best-fit power law,  $L(\Phi)dL \propto L^{-\alpha}dL$  (straight line). The fit was computed by least squares in  $(M_V, \log N_{cl})$  space with weights proportional to  $N_{cl}$ , the number of clusters per bin.

The lowest-luminosity bin was given zero weight because of the incomplete number of clusters in it.

As a check and because of the small numbers of clusters involved, we also binned clusters into constant-number bins of varying widths (2 bins with 5 clusters each for the brightest clusters, plus 9 bins with 10 clusters each for the remainder). For each bin, the number of clusters per unit magnitude,  $\nu_{cl}$ , was computed by dividing the number of clusters by the bin width. Figure 12b shows the resulting LF plotted logarithmically vs  $M_V$  and the best-fit power law derived from it in a similar fashion as above,  $L(\Phi)dL \propto L^{-1.77 \pm 0.12}dL$ . Obviously, the two derived power laws agree to well within the errors of their exponents, and we adopt a mean value of  $-1.75 \pm 0.1$  for the exponent of the best fit.

The resulting LF for the young massive clusters of NGC 34,  $L(\Phi)dL \propto L^{-1.75 \pm 0.1}dL$ , is in good accord with the power laws found for cluster systems in many other merging and starburst galaxies. These power laws have an average exponent of  $-1.93$  with a scatter of  $\pm 0.18$  (Whitmore 2003).

### 3.5.3. Cluster Velocities

Table 6 gives the heliocentric radial velocities  $c_{z_{hel}}$  measured for five of the star clusters. These velocities represent averages of velocities measured by two different methods. First, we determined a mean velocity from 5–12 absorption lines (see  $N_{abs}$  in Col. 3) measured individually in each cluster spectrum. And second, we also determined a mean velocity for each cluster via cross-correlation. Since none of the velocity standards observed during the run matched the A-type cluster spectra well, we used as a template the spectrum of the cluster NGC 7252:W3 obtained years earlier with the Blanco 4-m telescope at similar resolution (Schweizer & Seitzer 1998). This cluster has a similar age and spectrum, and its radial velocity is known with high accuracy from *VLT*/UVES observations,  $c_{z_{hel}} = 4822.5 \pm 1.0$  km s $^{-1}$  (Maraston et al. 2004; cf. with  $4821 \pm 7$  km s $^{-1}$  by Schweizer & Seitzer 1998). Results from the two methods agreed to within the combined errors, and the velocities given in Table 6 represent a weighted average of the two mean velocities measured for each cluster.

Also given in Table 6 are the cluster velocities  $\Delta v$  relative to the nucleus of NGC 34. These relative line-of-sight (LOS) velocities were computed from

$$\Delta v = (c_{z_{hel}} - c_{z_{hel,sys}}) / (1 + z_{hel,sys}),$$

where the denominator is a relativistic correction and the systemic velocity of NGC 34 is  $c_{z_{hel,sys}} = 5870 \pm 15$  km s $^{-1}$  (§ 3.3). The values of  $\Delta v$  for the five clusters lie in the range  $-210 \lesssim \Delta v \lesssim +80$  km s $^{-1}$ , indicating that all five clusters are physically associated with NGC 34.

The estimated systemic velocity of the five clusters is  $5841 \pm 48$  km s $^{-1}$  and agrees to within  $< 1\sigma$  with the above systemic velocity of NGC 34. The cluster velocity dispersion estimated via the Pryor & Meylan (1993) maximum-likelihood method is at least  $100 \pm 36$  km s $^{-1}$ , yet remains very uncertain due to the small number of measured clusters and their one-sided projected spatial distribution.

The LOS velocities and apparent spatial alignment of clusters 3, 7, 13, and 2 provide strong evidence against these clusters rotating in a disk and some evidence in favor of halo-type motions. These four clusters lie along an apparent line extending from 2.3 kpc NNW of the nucleus to 2.7 kpc SE and reaching its closest distance of 0.8 kpc from the nucleus between clusters 7 and 13. Sequentially, the LOS velocities of

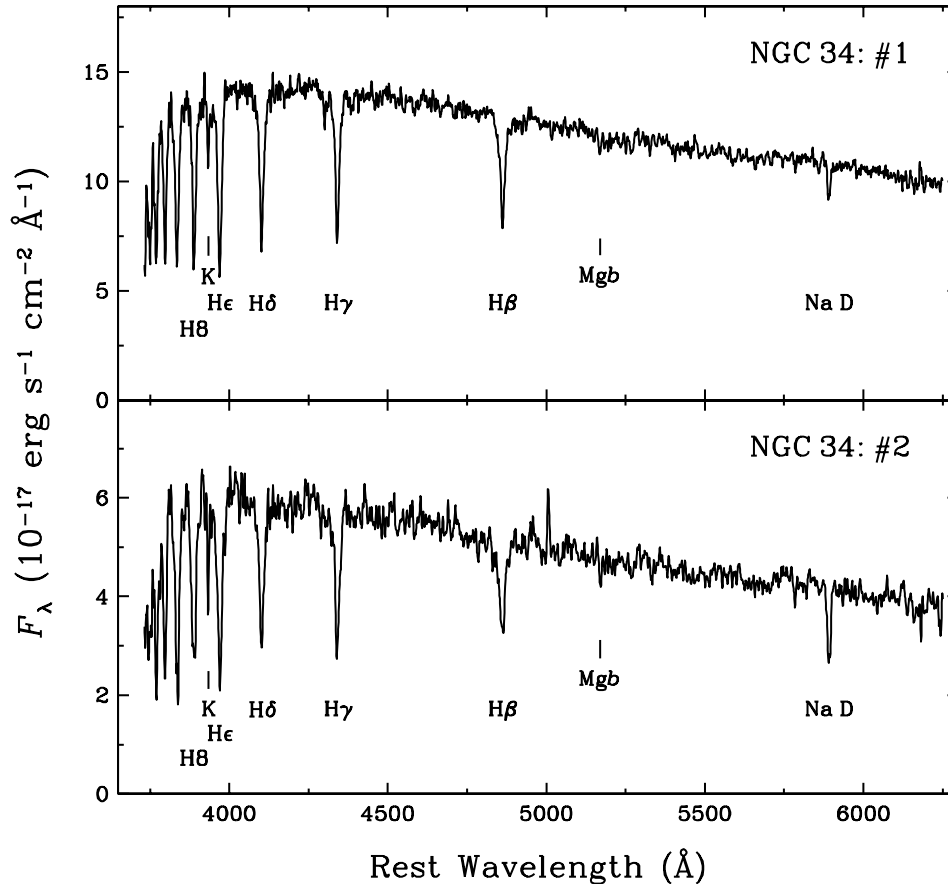


FIG. 13.— Ultraviolet-to-red spectra of clusters 1 and 2 in NGC 34, obtained with the Baade 6.5-m telescope and LDSS-2 spectrograph through a  $1''.03 \times 330''$  slit oriented at various position angles (see Table 1). The spectra are flux calibrated and plotted vs. rest wavelength. The spectrum of Cluster 2 has been slightly Gaussian smoothed ( $\sigma = 1.0 \text{ \AA}$ ) for better display. Note in both spectra the strong Balmer absorption lines indicative of A-type main-sequence stars. Cluster 2 also shows some residual  $[\text{O III}]\lambda\lambda 4959, 5007$  line emission and strong Na D absorption, both indicative of gas in its environment.

clusters 3, 7, 13, and 2 are  $+80, -210, +79,$  and  $-20 \text{ km s}^{-1}$ , respectively, suggesting the presence of random motions larger than any possible disk-rotation components.

#### 3.5.4. Cluster Ages and Metallicities

The two brightest of the five spectroscopically observed clusters yielded spectra of sufficient quality to permit a simple analysis of their likely ages and metallicities. Figure 13 displays the flux-calibrated spectra of these two clusters, numbers 1 and 2 in Table 4, plotted vs the rest wavelength. As pointed out above (§ 2.4), the strong Balmer absorption lines are indicative of A-type main-sequence stars, suggesting that both clusters have ages roughly in the range  $10^8$ – $10^9$  yr.

Given the spectra's relatively low signal-to-noise ratios, we have found it difficult to measure metal lines with the accuracy required for a reliable determination of the metallicities. Yet the Balmer absorption lines, which contain most of the age information, are strong and easily measured. Hence, we adopt a two-step procedure similar to the one used by Schweizer & Seitzer (1998). First, we assume that the clusters have approximately solar metallicities and determine their ages from three Balmer-line indices via comparison with model spectra computed for clusters of  $Z = Z_{\odot}$ . Then, we estimate the metallicities as best we can and check whether the assumption of solar metallicity is consistent with the observations.

To determine cluster ages and estimate metallicities, we measured 12 Lick line-strength indices—including  $H\beta$ ,

$H\gamma_A$ ,  $H\delta_A$ ,  $Mg b$ , and several Fe indices (Faber et al. 1985; Worthey & Ottaviani 1997; Trager et al. 1998)—from appropriately smoothed versions of the observed cluster spectra (i.e., smoothed to the  $\sim 8$ – $11 \text{ \AA}$  resolution of original Lick spectra). For comparison, we also measured indices for the nuclear spectrum. Table 7 presents the values of seven indices used in the final analysis, plus the index combination  $[\text{MgFe}]$  (see below) and logarithmic ages derived for the two clusters.

Figure 14 illustrates our derivation of cluster ages from the measured three Balmer-line indices  $H\beta$ – $H\delta_A$  and the broadband color  $(B-V)_0$ . The plotted curves show the predicted evolution of these four quantities as a function of logarithmic age, as computed by Bruzual & Charlot (2003, hereafter BC03) for model star clusters of logarithmic metallicities  $[Z] \equiv \log(Z/Z_{\odot}) = -0.4, 0.0,$  and  $+0.4$  relative to the sun.<sup>8</sup> To compare the observations with the models, the figure also shows the line indices and colors measured for clusters 1 and 2 as horizontal lines. The ages of these two clusters were then determined from the figure as follows. Logarithmic ages were read off at the intersections between the horizontal lines marking the measurements and the curves representing the model indices and color for  $[Z] = 0$ . Since for each cluster the Balmer-line indices yield two possible age values, the measured color index  $(B-V)_0$ —corrected for Milky-Way foreground reddening—was used to try to select the more likely of

<sup>8</sup> Using cluster models computed by Korn et al. (2005) instead of BC03 yields similar results.

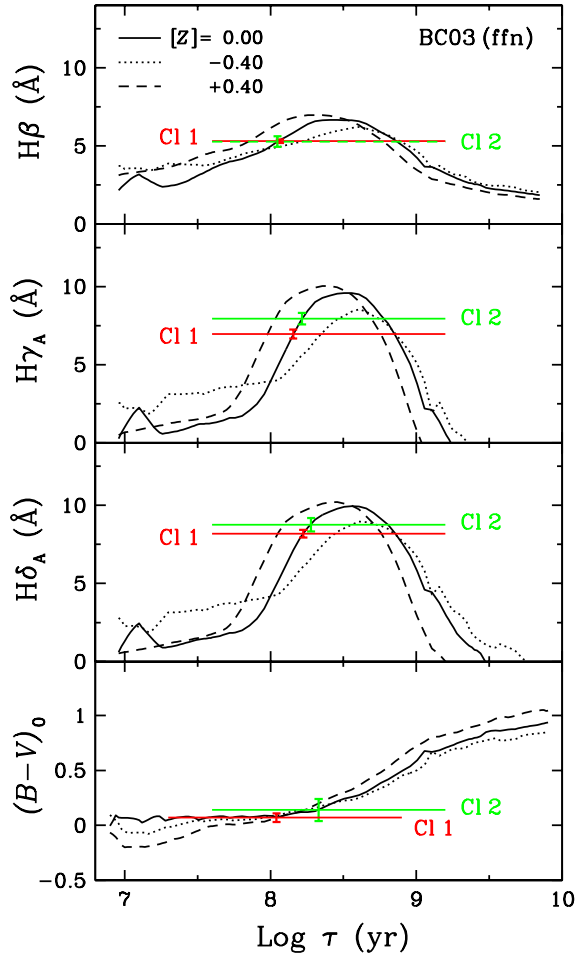


FIG. 14.— Evolution of the Lick indices  $H\beta$ ,  $H\gamma_A$ ,  $H\delta_A$  and color index  $(B-V)_0$  of model star clusters as a function of age  $\tau$  for three metallicities (solid, dotted, and dashed curves), compared with values measured for clusters NGC 34: 1 and 2 (horizontal lines). Note that the color index  $(B-V)_0$  favors the lower of two possible Balmer-line ages for each cluster and line index.

the two values. In each case, the color index seems to favor the younger of the two possible ages (especially when one considers that any correction for internal reddening in NGC 34 would yield a bluer intrinsic cluster color).

For Cluster 1, the value of  $(B-V)_0$  and its small error favor the younger age so clearly that we simply computed a weighted mean logarithmic age from the individual ages obtained for  $H\beta$ ,  $H\gamma_A$ , and  $H\delta_A$ . This mean logarithmic age, based on an assumed solar metallicity, is given in the last column of Table 7 and corresponds to a (linear) age of  $150 \pm 20$  Myr.

For Cluster 2, the situation is more complicated. The  $(B-V)_0$  color also favors the younger of two possible ages, yet various metal-line indices seem to point strongly toward the older age. We illustrate this with two figures containing diagnostic diagrams.

Figure 15 shows each of the three age-sensitive Lick indices  $H\beta-H\delta_A$  plotted vs the metallicity index  $[MgFe]$  (González 1993). This index is defined through  $[MgFe] \equiv [Mgb \times \frac{1}{2}(Fe5270 + Fe5335)]^{1/2}$ , where  $Mg\ b$ ,  $Fe5270$ , and  $Fe5335$  are Lick indices expressed in angstroms; it is nearly insensitive to variations in  $\alpha/Fe$ , the ratio of  $\alpha$ -elements to iron (Thomas et al. 2003). Besides the data points for the two clusters, each panel also displays evolutionary tracks for model

star clusters computed by BC03 for metallicities of  $[Z] = -0.7, -0.4, 0.0$ , and  $+0.4$ .<sup>9</sup> Whereas Cluster 1 appears to be young ( $< 300$  Myr) no matter what its exact metallicity is, Cluster 2 in these diagrams appears to be nearly 630 Myr old ( $\log \tau \approx 8.8$ ) and of slightly subsolar metallicity.

A similarly high age for Cluster 2 seems to be indicated by the observed strengths of three individual Fe-line indices, two of which have already been used in combination with the  $Mg\ b$  index above. Figure 16 plots the predicted and observed Lick indices  $H\beta$ ,  $Fe5015$ ,  $Fe5270$ , and  $Fe5335$  vs logarithmic cluster age. Whereas at its younger age Cluster 1 falls near or slightly below the solar-metallicity track on all three Fe-index diagrams, Cluster 2 falls well outside any evolutionary tracks in two of the three Fe-index diagrams. However, when plotted at its older age (as inferred from the Balmer-line indices) Cluster 2 falls within about a factor of two of the solar-metallicity tracks in all three Fe-index diagrams. Hence, for this cluster the higher mean logarithmic age given in Table 7, corresponding to an age of  $640 \pm 40$  Myr, seems to be at least as likely as the lower age of  $160 \pm 30$  Myr favored by the  $(B-V)_0$  index.

In conclusion, Cluster 1 seems definitely young ( $\sim 150$  Myr), while Cluster 2 could be similarly young but appears, from the strengths of its  $Mg$  and  $Fe$  lines, more likely to be about four times as old ( $\sim 640$  Myr). Both clusters seem to have metallicities compatible with our assumption of roughly solar metallicity.<sup>10</sup>

### 3.6. Parameters of NGC 34

To summarize the main results of § 3, Table 8 presents the relevant parameters of NGC 34 collected into one place.

## 4. DISCUSSION

The present discussion addresses various issues concerning the structure of NGC 34, the nature of its young massive clusters, and its gaseous outflow. It concludes with a description of the sequence of events that may have unfolded during the merger up to its present stage.

### 4.1. NGC 34: Remnant of a “Wet” Unequal-Mass Merger

NGC 34 exhibits several signatures that we have come to associate with mergers of gas-rich disks: two long main tidal tails, despite the galaxy’s relatively isolated position (§ 3.1); a single main body with an apparently single nucleus; plenty of  $H\ I$  and molecular gas,  $M_{H+H_2} = 1.2 \times 10^{10} M_\odot$  (§ 1 and Table 8); a starburst with a SFR of  $50\text{--}90 M_\odot \text{ yr}^{-1}$  (Valdes et al. 2005; Prouton et al. 2004); and, as an extra, a likely AGN. In addition, NGC 34 also features a remarkably blue, exponential stellar disk (§ 3.2) with a scale length of about 1.6 kpc (Table 5) and extending out to a radius of at least 10 kpc (Fig. 8).

Three questions of interest concerning the past merger are: (1) Is this blue exponential disk a surviving disk, or is it a new disk that formed from gas pooled during or after the merger? (2) What was the approximate mass ratio of the two disk galaxies that merged? And (3), has this merger essentially run to completion?

<sup>9</sup> Note that for clusters of age  $\lesssim 500$  Myr, the traditional grids of isochrones and isometallicity lines become severely jumbled, whereas evolutionary tracks yield a relatively clear picture.

<sup>10</sup> Note that we have avoided drawing any conclusions from the  $Ca\ II\ K$  and  $Na\ I\ D$  lines which may, especially in Cluster 2, feature significant nonstellar components due to NGC 34’s gaseous outflow (§ 3.4).



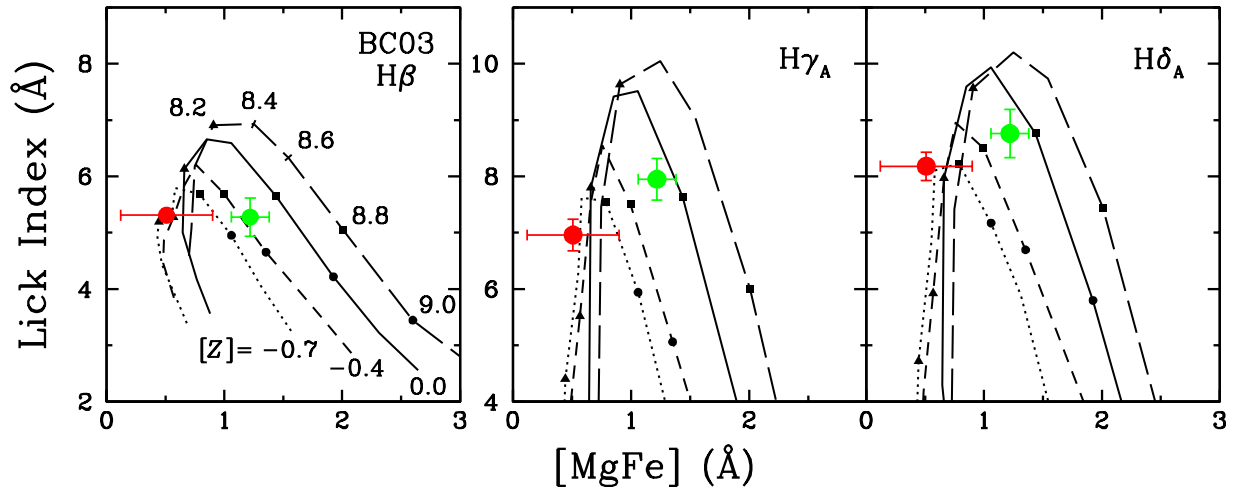


FIG. 15.—  $H\beta$ ,  $H\gamma_A$ , and  $H\delta_A$  vs  $[MgFe]$  diagrams for clusters 1 (red data points) and 2 (green) in NGC 34. Evolutionary tracks computed by BC03 for model star clusters of metallicities  $[Z] = -0.7, -0.4, 0.0,$  and  $+0.4$  (long dashes) are shown for comparison, with selected logarithmic ages marked along each track. From these diagrams Cluster 1 appears to be definitely young ( $<300$  Myr), though of ill determined metallicity, while Cluster 2 appears to be about 600 Myr old and of slightly subsolar metallicity.

In trying to address the first question, we note that the prominence of the exponential disk diminishes strongly from  $B$  to  $I$ , and the disk is undetectable in the  $K$  surface-brightness profile measured by RJ04 (§ 3.2). This suggests that the disk consists mainly of stars younger than  $\sim 1$  Gyr, since any significant older stellar component of the disk should show in the  $K$  profile. The position of the disk in the  $(B-V)_0$  vs  $(V-I)_0$  two-color diagram shown in Fig. 17 supports this hypothesis and allows us to estimate the age of the stellar component that dominates the optical light of the disk.

Shown in this diagram are evolutionary tracks for single-burst stellar populations (SSP) of metallicities  $[Z] = 0$  and  $-0.4$  computed by BC03 and the colors of the best-fit exponential disk (blue filled and open circle) and spheroid (red circles). The filled circles mark the disk and spheroid colors for the best-fit model with a full exponential disk, while the open circles mark the corresponding colors for the best-fit model with a disk that has a central hole (see § 3.2). The fact that in both cases the location of the disk in the two-color diagram falls close to the SSP tracks suggests that the disk light may, indeed, be dominated by a postburst population with perhaps a relatively narrow age spread. Projecting the two disk locations perpendicularly onto the model evolutionary tracks yields single-burst disk ages of  $\tau_{\text{eD}} \approx 380 \pm 50$  Myr for  $[Z] = 0$  and  $440 \pm 50$  Myr for  $[Z] = -0.4$ , respectively, where the estimated errors reflect uncertainties in metallicity and extinction, but not in the systematics of the model.

How massive is this disk, if indeed it formed mainly over a relatively short period about 400 Myr ago? With a mass-to-light ratio of  $M/L_V = 0.22 \pm 0.02 (M/L_V)_\odot$  for an SSP of  $[Z] = 0$  and the above age  $\tau_{\text{eD}}$  (BC03), the absolute magnitudes of the best-fit model disk translate into disk masses of  $M_{\text{eD}} = (3.3 \pm 0.3) \times 10^9 M_\odot$  for the full disk and  $(2.1 \pm 0.2) \times 10^9 M_\odot$  for the disk with a central hole, respectively. These estimated disk masses represent only about 27% and 17%, respectively, of the total mass of cold gas still present in NGC 34 ( $M_{\text{HI}+\text{H}_2} = 1.2 \times 10^{10} M_\odot$ , see § 1). Hence, this blue disk may well have formed from gas pooled in the late stages of the merger.

This brief discussion is not meant to exclude the possibility that the stellar disk may, at a diminished rate, continue to grow even at the present time. Upon visual inspection of the *HST*-archival  $V$  image one can see a close correspondence be-

tween some of the young star clusters and their surrounding dust lanes and knotty luminous filaments. This correspondence suggests that, especially near the two major dust lanes that may connect the inner disk to the outer tails (§ 3.1), stars and clusters may still be forming and, therefore, adding to the disk’s stellar mass.

In trying to address the second question, concerning what the approximate mass ratio of the two input disk galaxies may have been, we note that there are at least three clues.

First, the blue exponential disk—being most likely newly formed rather than a surviving structure—suggests that the merger leading to NGC 34 must have been close to being a major merger (here defined as  $m/M \gtrsim 1/3$ ), or else the dominant of the two old-star disks would have partially survived (e.g., Barnes 1998; Naab & Burkert 2003). Therefore, a clearly minor merger with  $m/M < 1/4$  seems unlikely, and the lack of a moderately massive old disk places a lower limit of  $\sim 0.3$  on the mass ratio of the two input galaxies.

Second, the fact that the N tail appears significantly brighter than the S tail argues against a major merger of two nearly equal-mass disks, making a mass ratio close to 1:1 seem unlikely. By exclusion, then, the likely mass ratio of the two input disks must have been somewhere in the range  $1/3 \lesssim m/M \lesssim 2/3$ .

Third, another morphological feature of NGC 34 also seems to argue for a mass ratio approximately in the above range. On high-contrast displays (e.g., Figs. 1a and 1e) NGC 34 appears unlike either of the two classical remnants of nearly equal-mass mergers, NGC 7252 (Schweizer 1982; Hibbard & Mihos 1995) and NGC 3921 (Schweizer 1996). Rather, NGC 34 appears to have grafted onto it a low-surface-brightness cloud of debris (the NW Cloud, see § 3.1), from which emerge at least one, and possible two, faint tail-like features. Model simulations of unequal-mass disk mergers with gas (e.g., Barnes 2002; Naab et al. 2006) suggest that up to four tidal tails may form and coexist in direct  $m/M = 1/3$  mergers, with “each [tail] originating from a different disk at a different passage” (Barnes 2002, esp. Fig. 5). This situation may, in fact, correspond to the present configuration in NGC 34 and would seem to support a recent merger of mass ratio  $\sim 1/3$ .

Independent support for this conclusion comes from the

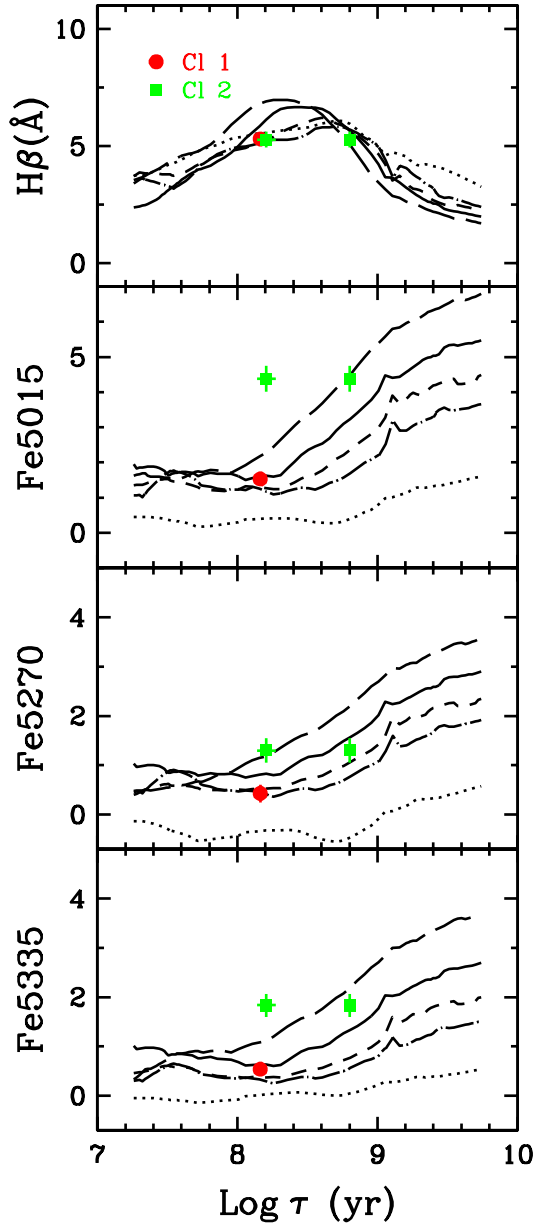


FIG. 16.— Lick spectral indices  $H\beta$ , Fe5015, Fe5270, and Fe5335 measured for clusters 1 and 2 in NGC 34 and compared with spectral evolution models by BC03 for clusters of five different metallicities:  $[Z] = -1.7$  (dotted curves),  $-0.7$ ,  $-0.4$ ,  $0.0$ , and  $+0.4$  (long-dashed curves). The data points for Cluster 1 are plotted at the logarithmic age given in Table 7, while those for Cluster 2 are plotted at both the low and high logarithmic ages given in that table. If one adopts the high age for Cluster 2, both clusters have roughly solar metallicities to within a factor of about 2–3; for details, see § 3.5.4.

global kinematics of the remnant. In a diagram plotting a measure of rotational support,  $(V_{\text{rot}}/\sigma)^*$ , versus the isophotal-shape parameter  $\bar{a}_4/a$ , NGC 34 clearly falls in the quadrant of rotationally supported, disk merger remnants (Rothberg & Joseph 2006b, esp. Figs. 4 and 5). Simulations of disk–disk mergers with gas by Naab et al. (2006) suggest that remnants of mergers with mass ratios of  $m/M \approx 1/3$  populate the region of the diagram containing NGC 34, whereas remnants of 1:1 mergers do not.

Finally, the third question of interest concerns the current stage of the disk–disk merger in NGC 34. Specifically, has the merger in this galaxy essentially run to completion? Given the observed strong nuclear outflow (§ 3.4) and general evi-

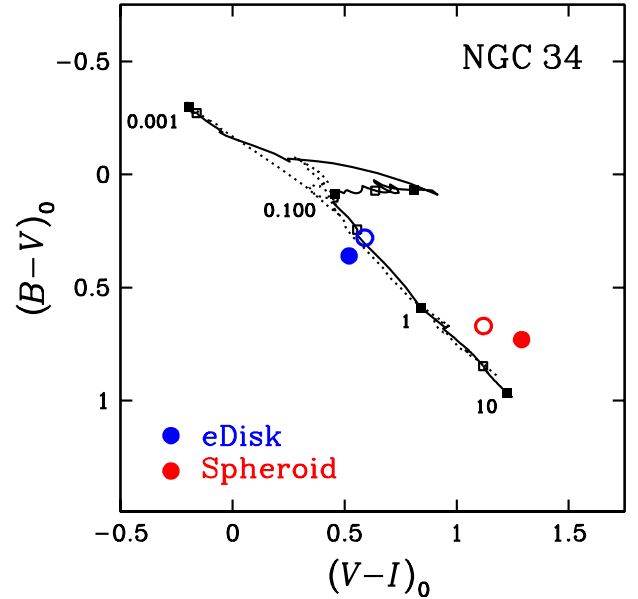


FIG. 17.— Two-color diagram comparing the  $(B-V)_0, (V-I)_0$  colors of NGC 34’s exponential disk and spheroid with evolutionary tracks for single-burst stellar populations of metallicity  $[Z] = 0$  (solid line) and  $-0.4$  (dotted line) computed by BC03. The filled squares along the solar-metallicity track mark population ages of 0.001, 0.010, 0.100, 1, and 10 Gyr, while the open squares mark ages of 0.003 to 3 Gyr. The two filled color dots indicate the locations of the best-fit model spheroid and disk without central hole, while the two open circles indicate those for the best-fit model spheroid and disk with a central hole. (The dot sizes correspond to about  $\pm 2\text{-}\sigma$  errors in the color indices.) Note that regardless of the absence or presence of a central hole, the disk colors suggest a single-burst disk age of approximately 400 Myr.

dence that starburst-induced outflows may peak around the time when the two nuclei coalesce (e.g., Cox et al. 2006), the presence or absence of a second nucleus should help us discern just how advanced the current stage of this merger is.

Despite a past claim for a second nucleus in NGC 34 (Miles et al. 1996), we have found no evidence for it and can put some strong limits on its maximum brightness in the  $K$  band. Early observations at  $10\ \mu\text{m}$  showed a very compact, slightly North–South elongated mid-IR source at the nucleus with a full width at half maximum of  $\lesssim 1''.7 \times 2''.3$  (Keto et al. 1991) or  $\lesssim 700 \times 950$  pc at our adopted distance. A radio continuum map obtained at 8.44 GHz with the VLA and a  $0''.25 \times 0''.40$  beam shows an essentially unresolved central source, with possibly a second, much weaker source about  $1''.2$  south (Fig. 1 in Condon et al. 1991). This second source is not explicitly mentioned by Condon et al. and, being  $\sim 300\times$  weaker than the primary source, can hardly be counted as evidence for a second nucleus.

The only positive evidence for a second nucleus stems from mid-IR observations at  $8.8\ \mu\text{m}$  and  $12.5\ \mu\text{m}$  carried out with SpectroCam-10, a diffraction-limited mid-IR camera, at the Palomar 5-m telescope (Miles et al. 1996). These observations suggested the presence of a second mid-IR source about  $1''.2$  south of the primary nucleus, with a claimed brightness ratio of  $\sim 0.6$  at  $8.8\ \mu\text{m}$  and  $\sim 0.4$  at  $12.5\ \mu\text{m}$  relative to the primary nucleus. Deconvolutions seemed to enhance the secondary nucleus and its similarity with the possible secondary 8.44 GHz radio source (see Figs. 4 and 5 in Miles et al.), yet the data clearly had a low signal-to-noise ratio and the reality of the second source seems doubtful.

We have conducted a search of NICMOS  $K$ -band images of NGC 34 available via the *HST* Archive and have found

no trace of any secondary nucleus  $\sim 1''/2$  south of the primary one. Specifically, measurements on the  $K$ -band exposure N49J21080 (camera NIC2, filter F205W, exposure time 512 s, program GO-7268, PI: van der Marel), which nicely shows many of the young massive star clusters, demonstrate that any secondary nucleus—if present—must be  $\gtrsim 7.0$  mag fainter in  $K$  than the primary nucleus is. Thus, if really a second nucleus existed and was of an intrinsic luminosity comparable to that of the primary nucleus, it would have to suffer an additional extinction of  $A_K \gtrsim 7.0$  mag, corresponding to an additional visual extinction of  $A_V \gtrsim 65$  mag.

Although we cannot exclude this possibility, we conclude that—at least at present—there is no good evidence for a second nucleus of any significance. The merger in NGC 34 likely has run past the stage of the two nuclei coalescing and is, therefore, essentially complete.<sup>11</sup>

In short, as best as we can tell NGC 34 appears to be the remnant of a gas-rich (“wet”) merger between two disk galaxies with a mass ratio likely in the range  $1/3 \lesssim m/M \lesssim 2/3$ . Out of the pooled gas of the two input galaxies a new exponential disk of stars has formed, and perhaps continues forming. As judged by the absence of any detectable second nucleus, the merger must essentially have run to completion.

#### 4.2. Nature of NGC 34’s Young Massive Clusters

Another signature of a recent gas-rich merger in NGC 34 are the many luminous young star clusters (§ 3.5). As a whole, these clusters resemble the young globular-cluster systems observed in other recent merger remnants, including NGC 3597 (Holtzman et al. 1996; Carlson et al. 1999), NGC 3921 (Schweizer et al. 1996, 2004), and NGC 7252 (Miller et al. 1997; Schweizer & Seitzer 1998; Maraston et al. 2001). The system includes about 140 luminous clusters ( $M_V \lesssim -9.3$ ) whose surface number density tracks the underlying galaxy light in  $V$  remarkably well. The system’s effective radius,  $r_{\text{eff,cl}} \approx 2.6\text{--}3.1$  kpc (§ 3.5.2), is typical for globular-cluster systems both young and old, while the clusters’ power-law LF,  $L(\Phi)dL \propto L^{-1.73 \pm 0.10}dL$ , is typical for young cluster systems (e.g., Whitmore 2003). Given the presence of a newly-formed, young stellar disk in NGC 34 (§ 4.1), an interesting question is whether this cluster system displays disk or halo kinematics. From five clusters with measured velocities, there is tentative evidence that the kinematics is that of a halo population (§ 3.5.3), but many more cluster velocities are needed to answer the question in a definitive manner.

The age distribution of the luminous clusters of NGC 34 is of great interest in trying to understand the star formation history of this recent merger remnant. In the absence of measured color indices for most clusters, our current information on ages stems mainly from the spectra available for five clusters. The strong Balmer absorption lines in these spectra suggest that all five clusters have ages in the range of about 0.1–1.0 Gyr and are, therefore, young. Young ages for most clusters are also indicated by the fact that nearly 3/4 of the detected candidate clusters (87 out of 117) have absolute magnitudes in the range  $-10.0 \geq M_V \geq -15.4$ , while at most a few percent of *old* globular clusters are typically more luminous than  $M_V = -10.0$ .

<sup>11</sup> The NW Cloud, regarded by some as a second galaxy, contains  $\ll 1\%$  of the total luminosity of NGC 34 in the  $I$  band and has no visible nucleus. Likely, it is either a tidal fragment of one of the two previous disk galaxies or else an interacting dwarf companion galaxy unrelated to the main recent merger event in NGC 34.

At present, we cannot determine whether—within the 0.1–1.0 Gyr age interval—the young clusters of NGC 34 have a relatively wide or narrow age distribution. Of all candidate clusters, only the two most luminous have individually determined ages. As described in § 3.5.4, there is a possibility that both of these clusters have ages of about 130–190 Myr, although it looks more likely that Cluster 1 is about  $150 \pm 20$  Myr old and Cluster 2 about  $640 \pm 40$  Myr old. The first possibility would suggest that cluster formation may have peaked sharply in the recent past, while the more likely second possibility suggests that cluster formation may have been drawn out over  $\sim 0.5$  Gyr or may have occurred in two or more bursts. Additional photometry and spectroscopy are needed to shed light on this important issue.

What are the likely masses of the young star clusters? For the two most luminous clusters, we can estimate photometric masses from their absolute visual magnitudes and spectroscopic ages. For Cluster 1, the photometric mass is  $(15 \pm 1) \times 10^6 M_\odot$  when derived from BC03 models with a Chabrier (2003) IMF and  $(19 \pm 2) \times 10^6 M_\odot$  when derived from Maraston (2005) models with a Kroupa (2001) IMF. Hence, this cluster is about 3–4 times more massive than  $\omega$  Cen, the most massive GC in the Milky Way [ $M_{\omega \text{ Cen}} \approx (4 \pm 1) \times 10^6 M_\odot$ , Meylan 2002]. For Cluster 2, the corresponding photometric masses are about  $(20\text{--}24) \times 10^6 M_\odot$  (or 5–6  $M_{\omega \text{ Cen}}$ ) if the cluster is  $\sim 640$  Myr old, and about  $(9\text{--}11) \times 10^6 M_\odot$  (or 2–3  $M_{\omega \text{ Cen}}$ ) if it is only  $\sim 160$  Myr old. Hence, both clusters clearly are young *massive* clusters (YMCs), often understood to be clusters of mass  $\gtrsim 10^5 M_\odot$ . By association, presumably most of the 87 candidate clusters more luminous than  $M_V = -10$  are YMCs as well.

Are the YMCs of NGC 34 gravitationally bound and, therefore, genuine young globular clusters?

Although we have not attempted to measure effective radii for these clusters from the one available archival *HST*/WFPC2  $V$  exposure, we have measured their apparent full widths at half maximum with the IRAF task *imexamine* and have compared the values with widths similarly measured for the young globular clusters S1 and S2 in NGC 3921 (Schweizer et al. 1996), a merger remnant at nearly the same redshift distance as NGC 34. In both cases, the measurements were made from  $V$  exposures taken with the Planetary Camera (PC) of WFPC2 within eight months of each other. The apparent widths of the five NGC 34 clusters observed spectroscopically are a few percent smaller than the apparent widths of clusters S1 and S2 in NGC 3921, which both have measured effective radii of  $r_{\text{eff}} \lesssim 5$  pc (Schweizer et al. 2004). Hence, the YMCs of NGC 34 very likely have effective radii of  $\lesssim 5$  pc as well, radii that are typical for globular clusters.

Given these normal effective radii and the estimated ages of  $\gtrsim 10^8$  yr, corresponding to at least 25–50 internal crossing times ( $t_{\text{cr}} \approx 2\text{--}4$  Myr), all five NGC 34 clusters observed spectroscopically must be gravitationally bound and are, therefore, *massive* ( $\gtrsim 2 \times 10^6 M_\odot$ ) *young globular clusters*.

These clusters are likely to be long-lived. Most of the early mass loss due to supernovae and stellar evolution, which can disrupt very young clusters, occurs during the first  $\sim 100$  Myr (e.g., Fall & Zhang 2001; Boily & Kroupa 2003). Since the five NGC 34 clusters are all older than 100 Myr, yet of normal compactness, they have already survived their most disruption-prone period and are likely to survive for at least several Gyr and perhaps a Hubble time or longer (e.g., Baumgardt 2006, esp. Fig. 3). Their individual lifetimes will depend, in part, on their orbits and—especially—on whether

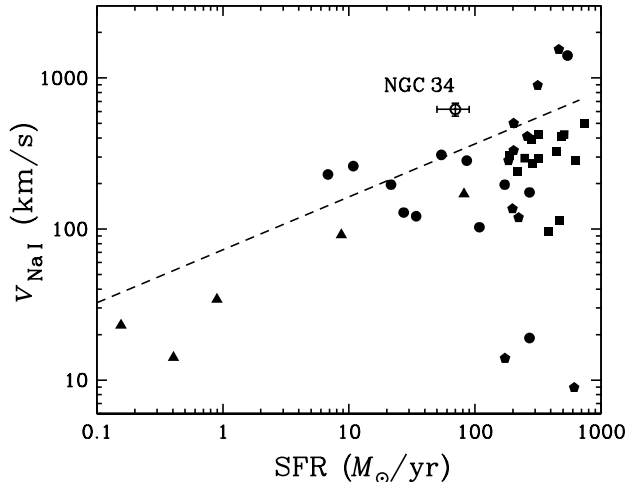


FIG. 18.— Mean (center-of-line) velocity of the Na I outflow in NGC 34 compared to similar velocities for a sample of 41 starburst galaxies assembled by Martin (2005b). The mean outflow velocities  $v_{\text{Na I}}$  are plotted vs each galaxy’s star formation rate. The various data points represent ULIRGs (squares and pentagons), LIRGs (filled circles), and dwarf starburst galaxies (triangles), while the dashed line represents an upper-envelope fit taking projection effects into consideration (for details and references to data, see Martin 2005b, esp. § 4.2 and Fig. 6). Note the high mean Na I velocity of NGC 34’s outflow, exceeding the mean outflow velocities of all but three of the 24 more intensely star-forming ULIRGs.

they reside in the halo or the disk.

In summary, at least the five spectroscopically observed clusters of NGC 34 are genuine, massive young globular clusters with long expected lifetimes. What fraction of the other 82 YMCs more luminous than  $M_V = -10$  can be described in a similar fashion depends on their individual ages and thus remains unknown at present.

#### 4.3. NGC 34’s Outflow

As revealed mainly by the strong blueshifted D lines of Na I, the center of NGC 34 drives a strong outflow of cool, neutral gas with a mean (i.e., center-of-line) velocity of  $v_{\text{Na I}} = -620 \pm 60 \text{ km s}^{-1}$  and a maximum detected velocity of about  $-1050 \pm 30 \text{ km s}^{-1}$  (§ 3.4). Much lower net outflow velocities averaging about  $-75 \text{ km s}^{-1}$  are also observed in the ionized gas. As far as we can tell from the spectra of clusters 3 and 7, the Na I outflow seems to extend northward of the nucleus in a fan-like structure out to at least  $\sim 2.3 \text{ kpc}$  NNE in the case of Cluster 3.

Our discovery of this outflow is hardly surprising given the estimated SFR of  $70 \pm 20 M_{\odot} \text{ yr}^{-1}$  in NGC 34 (§ 1). While most *ultraluminous* infrared galaxies (ULIRGs) feature strong gaseous outflows, many LIRGs also feature similar, though weaker, outflows (e.g., Heckman et al. 2000; Martin 2005a; Veilleux et al. 2005). It appears that most galaxies with centrally concentrated star formation in excess of  $\sim 10 M_{\odot} \text{ yr}^{-1}$  may drive some form of Na I outflow, regardless of whether they contain an AGN or not (Rupke et al. 2005).

What is perhaps surprising about the Na I outflow of NGC 34 is its relatively high mean and maximum velocities. Figure 18 shows the mean outflow velocity (data point with error bars) plotted in a diagram of  $v_{\text{Na I}}$  vs SFR for 41 starburst galaxies assembled by Martin (2005b, esp. Fig. 6). These galaxies represent the highest surface-brightness objects in their luminosity class and are thought to outline the highest mean outflow velocities. The dashed line represents an upper-envelope fit made via a simple model of projection

effects (for details, see Martin 2005b). The figure suggests, then, that the neutral-gas outflow of NGC 34 is exceptionally strong for the estimated SFR of  $70 \pm 20 M_{\odot} \text{ yr}^{-1}$ . Even when compared to Na I outflows in ULIRGs, this outflow has an unusually high mean velocity: Whereas the SFRs of the 15 ULIRGs with outflows detected by Martin (squares in Fig. 18),  $190 \lesssim \text{SFR} \lesssim 750 M_{\odot} \text{ yr}^{-1}$ , are 2–10 $\times$  higher than the SFR of NGC 34, the mean outflow velocities of these ULIRGs lie in the range 60–500  $\text{km s}^{-1}$ , while the corresponding velocity measured for NGC 34 is  $|v_{\text{Na I}}| = 620 \pm 60 \text{ km s}^{-1}$ .

Despite this ongoing high-velocity outflow there is still plenty of cool gas left in NGC 34 ( $M_{\text{HI+H}_2} = 1.2 \times 10^{10} M_{\odot}$ , see § 1), and an additional significant amount of cool gas has already been converted into a young stellar disk (§ 4.1). Even with its infrared luminosity of  $L_{\text{IR}} \approx 10^{11.5} L_{\odot}$  NGC 34 is clearly not in the league of the most luminous infrared galaxies ( $L_{\text{IR}} > 10^{12} L_{\odot}$ ) where AGNs may—according to an increasingly widely held view—scour remnants free of gas so efficiently as to rapidly suppress all star formation. Specifically, the transition to this extreme regime may occur for very massive remnants with velocity dispersions of  $\sigma_v \approx 240 \text{ km s}^{-1}$  (Schawinski et al. 2006), while NGC 34 has only  $\sigma_v = 201 \pm 8 \text{ km s}^{-1}$  (Rothberg & Joseph 2006a). Hence, the galaxy’s cool-gas mass, SFR, and depth of the potential well are all consistent with each other.

Perhaps the most interesting lesson contributed by NGC 34 is that the sequence of various events may matter. As we are about to discuss, the outflow of cool gas in this galaxy seems to be occurring toward the end of the main starburst and after the gas has settled into a major new disk.

#### 4.4. Sequence of Events

With a strong outflow of cool gas under way in NGC 34, it is of interest to establish what events preceded it during the recent merger.

Summarizing our findings, the spatially extended phase of the merger-induced starburst seems to have peaked more than  $\sim 100 \text{ Myr}$  ago, giving birth to a system of genuine young globular clusters with ages approximately in the range 0.1–1.0 Gyr (§ 4.2). From gas settling into a disk toward the end of the merger (e.g., Barnes 2002), a new stellar disk formed perhaps as much as  $\sim 400 \text{ Myr}$  ago (§ 4.1). A similar age is inferred from the optical nuclear spectrum, which suggests a 300–400 Myr old poststarburst population surrounding the highly obscured nucleus proper. The lack of any detectable second nucleus suggests that the nuclei of the two participant galaxies of mass ratio  $1/3 \lesssim m/M \lesssim 2/3$  have coalesced. Yet, there still is a strong gaseous outflow. Therefore, *if* this outflow is of relatively short duration (say,  $\lesssim 50 \text{ Myr}$ ), then it is occurring *after* most of the merger processes have run to completion.

We now elaborate on some details of this sketchy scenario.

First, although the present cluster photometry does not allow us to exclude that some massive clusters may still be forming, the fact that five of the most luminous clusters all appear spectroscopically older than  $\sim 100 \text{ Myr}$  strongly suggests that the main cluster-formation epoch, and hence the peak of the galaxy-wide starburst, is over. If there were younger clusters of similar mass, they should—after all—be more luminous, yet they do not seem to be numerous among the brightest clusters.

Second, similar things can be said about the young stellar disk. Although it may still be forming stars at a diminished

rate, it looks surprisingly smooth and appears to be at a more advanced evolutionary stage than, e.g., the intensely star-forming central disk (“mini-spiral”) of NGC 7252 (Schweizer 1982; Whitmore et al. 1993; Miller et al. 1997). The sheer existence of this smooth young disk in NGC 34 and its classical exponential structure make it seem unlikely that a strong, gas-depleting outflow coexisted during the disk’s main formation period a few 100 Myr ago. Hence, like cluster formation disk formation seems to have largely preceded the present-day strong gaseous outflow.

Finally, although the nuclei appear to have coalesced, there is no firm evidence as to exactly when this final phase of the merging process occurred. Yet, the exceptionally high central  $H$ -band luminosity density measured in NGC 34 (van der Marel & Zurek 2000), supported by a strong trend toward redder central colors (Figs. 6 and 7), suggests that a highly obscured central starburst, likely paired with a weak AGN (§ 1), is still occurring. If so, the nuclei may either still be in the last throes of their coalescence (<50 pc apart) or may have coalesced just recently, creating the final, concentrated starburst (and AGN) that drives the present outflow. This, then, seems to us the most likely explanation of the combined observations.

One interesting speculation is that—dynamical friction being weaker and acting more slowly in unequal-mass mergers than in equal-mass mergers—the seemingly late phase of strong gaseous outflow observed in NGC 34 may be a relatively normal consequence of the 1/3 – 2/3 mass ratio between the two galaxies that merged.

Whatever the exact interpretation and assuming that gaseous outflows peak for relatively brief periods, the indications seem strong that at least in NGC 34 the current outflow follows the main, galaxy-wide starburst, follows disk rebuilding, and may either immediately follow or be concurrent with the coalescence of the two nuclei.

## 5. SUMMARY

We have described imaging, photometric, and spectroscopic observations of the merger remnant NGC 34 (Mrk 938) obtained with the Baade and du Pont telescopes at Las Campanas, as well as the photometric analysis of an archival 500 s exposure in  $V$  obtained with the *HST*/WFPC2 camera. NGC 34 has often been classified as a Sey 2, but its nuclear spectrum is presently thought to be dominated by a highly obscured starburst, with a likely weak AGN contribution. The main results of our observations and analysis are as follows:

1. NGC 34 is relatively luminous ( $M_V = -21.6$  for  $H_0 = 70$ ) and situated at a distance of 85.2 Mpc ( $cz_{\text{hel}} = 5870 \pm 15$  km s<sup>-1</sup>). The galaxy features a single, very red nucleus, a main spheroid containing a prominent blue central disk and much outer fine structure, and a pair of tidal tails of unequal length and surface brightness, suggestive of two former disk galaxies of unequal mass. These galaxies appear to have completed merging. The remnant now features a rich system of young massive clusters, the above-mentioned blue exponential disk, and a strong gaseous outflow, all signatures of a recent gas-rich merger accompanied by a strong starburst.

2. NGC 34’s system of candidate young star clusters comprises about 140 objects more luminous than  $M_V \approx -9.3$ . Their surface number density tracks the underlying galaxy light in  $V$  closely, and their luminosity function is a power law typical of young cluster systems,  $L(\Phi)dL \propto L^{-1.73 \pm 0.10} dL$ . Of the 117 directly detected candidate clusters, 87 have absolute magnitudes in the range  $-10.0 \geq M_V \geq -15.4$ . Among

the most luminous clusters, five observed spectroscopically all feature strong Balmer absorption lines indicative of ages of  $\sim 0.1$ – $1.0$  Gyr. They have estimated photometric masses of  $2 \times 10^6 \lesssim M \lesssim 2 \times 10^7 M_\odot$  (for a Chabrier or Kroupa IMF) and are gravitationally bound young globulars. Their systemic kinematics seems to be dominated by relatively large random motions rather than by disk rotation, but velocities of more and spatially better distributed clusters will be needed to check this tentative result. Finally, the cluster system’s effective radius,  $r_{\text{eff,cl}} \approx 2.6$ – $3.1$  kpc, is typical for globular-cluster systems both young and old.

3. NGC 34’s prominent central disk turns out to be exponential and can be traced, via surface-brightness profile decomposition, out to at least 10 kpc radius. Its smooth structure and blue colors,  $(B-V)_{\text{eD},0} \approx 0.36$  and  $(V-I)_{\text{eD},0} \approx 0.52$ , suggest that its optical light may be dominated by a poststarburst stellar population about 400 Myr old. This disk contributes  $\sim 51\%$ ,  $43\%$ , and  $27\%$  of the total  $B$ ,  $V$ , and  $I$  light, respectively, if one assumes that it has no central hole, and about 2/3 of these values if one assumes that it does have a central hole. In either case, because of its youth this exponential disk contributes significantly to the total optical luminosity of NGC 34 even though its mass may be relatively modest ( $2$ – $4 \times 10^9 M_\odot$  if  $\sim 400$  Myr old).

4. As discovered from the broad blueshifted D lines of Na I, the center of NGC 34 drives a strong outflow of cool, neutral gas. The center-of-line velocity of this gas is  $v_{\text{Na I}} = -620 \pm 60$  km s<sup>-1</sup>, while the maximum detected velocity reaches about  $-1050 \pm 30$  km s<sup>-1</sup>. These outflow velocities are unusually high for a galaxy with an infrared luminosity of  $L_{\text{IR}} \approx 10^{11.5} L_\odot$  and estimated SFR of  $70 \pm 20 M_\odot \text{ yr}^{-1}$ . Much lower net outflow velocities averaging about  $-75$  km s<sup>-1</sup> are also observed in the ionized gas. We note that—since blueshifted Na D lines are also seen in two of the cluster spectra—future detailed mapping of the cool-gas outflow should be feasible via multi-object cluster spectroscopy.

5. The available morphological and structural evidence suggests that NGC 34 is the likely remnant of two recently merged gas-rich disk galaxies that had an estimated mass ratio of  $1/3 \lesssim m/M \lesssim 2/3$ . While the merger proceeded, a galaxy-wide starburst seems to have formed the young massive clusters beginning perhaps  $\sim 600$  Myr ago and the young exponential disk beginning shortly thereafter. By now, the two merging galaxies’ nuclei appear to have coalesced, the starburst has shrunk to a highly obscured central region of  $\lesssim 1$  kpc radius, and there is a strong gaseous outflow. The outflow’s high velocity may indicate that the obscured central starburst, and perhaps also the AGN activity, may be at or near their peak strengths.

We close with an educated guess: Given the presence of a young stellar disk and of  $\sim 1.2 \times 10^{10} M_\odot$  of cool gas that seems unlikely to be entirely blown away in the future (§ 4.3), NGC 34 may—over the next few Gyrs—turn into a bulge-dominated Sa galaxy akin to, though less massive than, The Sombrero (NGC 4594).

We thank Christopher Mihos for drawing our attention to NGC 34; Herman Olivares, Felipe Sánchez, and Hernán Núñez for expert assistance at the telescopes; Frank Valdes and Michael Fitzpatrick from the former IRAF Help Desk at NOAO for their steady support; Ivo Busko for his kind help with the STSDAS fitting package; Pieter van Dokkum for making available his cosmic-ray removal software; Gus-

tavo Bruzual and Stéphane Charlot for the early release of their latest cluster-evolution models; and Mark Phillips, Barry Madore, and Jane Rigby for helpful discussions. This research has benefited greatly from use of the NASA/IPAC Extragalactic Database (NED), which is operated by the Jet Propulsion Laboratory, California Institute of Technology, un-

der contract with NASA. One of us (F.S.) acknowledges partial support from the NSF through grants AST-99 00742 and AST-02 05994. This paper is dedicated to the memory of Horace W. Babcock, who envisioned, founded, and developed the Las Campanas Observatory.

## REFERENCES

- Afanasev, V. L., Lipovetskii, V. A., Markarian, B. E., & Stepanian, J. A. 1980, *Astrofizika*, 16, 193 (English transl. *Astrophysics*, 16, 119)
- Allington-Smith, J., et al. 1994, *PASP*, 106, 983
- Argyle, R. W., & Eldridge, P. 1990, *MNRAS*, 243, 504
- Baggett, W. E., Baggett, S. M., & Anderson, K. S. J. 1998, *AJ*, 116, 1626
- Barnes, J. E. 1998, in *Galaxies: Interactions and Induced Star Formation*, ed. D. Friedli, L. Martinet, & D. Pfenniger (Berlin: Springer), 275
- Barnes, J. E. 2002, *MNRAS*, 333, 481
- Barnes, J. E., & Hernquist, L. 1992, *ARA&A*, 30, 705
- Barnes, J. E., & Hernquist, L. 1996, *ApJ*, 471, 115
- Baumgardt, H. 2006, in *Globular Clusters—Guides to Galaxies*, ed. T. Richtler & S. S. Larsen (Berlin: Springer), in press (astro-ph/0605125)
- Boily, C. M., & Kroupa, P. 2003, *MNRAS*, 338, 673
- Bottinelli, L., Gouguenheim, L., Fouque, P., & Paturel, G. 1990, *A&AS*, 82, 391
- Bruzual A., G., & Charlot, S. 2003, *MNRAS*, 344, 1000 (BC03)
- Buchanan, C. L., et al. 2006, *AJ*, 132, 401
- Busko, I. C., & Steiner, J. E. 1990, *MNRAS*, 245, 470
- Carlson, M. N., et al. 1999, *AJ*, 117, 1700
- Chabrier, G. 2003, *PASP*, 115, 763
- Chini, R., Krügel, E., & Steppe, H. 1992, *A&A*, 255, 87
- Condon, J. J., Huang, Z.-P., Yin, Q. F., & Thuan, T. X. 1991, *ApJ*, 378, 65
- Corbett, E. A., et al. 2003, *ApJ*, 583, 670
- Cox, T. J., Di Matteo, T., Hernquist, L., Hopkins, P. F., Robertson, B., & Springel, V. 2006, *ApJ*, 643, 692
- da Costa, L. N., et al. 1998, *AJ*, 116, 1
- Dahari, O. 1985, *ApJS*, 57, 643
- de Vaucouleurs, G. 1953, *MNRAS*, 113, 134
- de Vaucouleurs, G., de Vaucouleurs, A., Corwin, H. G., Buta, R. J., Paturel, G., & Fouqué, P. 1991, *Third Reference Catalogue of Bright Galaxies* (Berlin: Springer)
- Faber, S. M., Friel, E. D., Burstein, D., & Gaskell, C. M. 1985, *ApJS*, 57, 711
- Fall, S. M., & Zhang, Q. 2001, *ApJ*, 561, 751
- Ferrarese, L., & Merritt, D. 2000, *ApJ*, 539, L9
- Gebhardt, K., et al. 2000, *ApJ*, 539, L13
- Goldader, J. D., Joseph, R. D., Doyon, R., & Sanders, D. B. 1997a, *ApJS*, 108, 449
- Goldader, J. D., Joseph, R. D., Doyon, R., & Sanders, D. B. 1997b, *ApJ*, 474, 104
- Gonçalves, A. C., Véron-Cetty, M.-P., & Véron, P. 1999, *A&AS*, 135, 437
- González, J. J. 1993, Ph. D. thesis, UC Santa Cruz
- Guainazzi, M., Matt, G., & Perola, G. C. 2005, *A&A*, 444, 119
- Hamuy, M., Walker, A. R., Suntzeff, N. B., Gigoux, P., Heathcote, S. R., & Phillips, M. M. 1992, *PASP*, 104, 533
- Heckman, T. M., Lehnert, M. D., Strickland, D. K., & Armus, L. 2000, *ApJS*, 129, 493
- Hibbard, J. E., & Mihos, J. C. 1995, *AJ*, 110, 140
- Hibbard, J. E., & van Gorkom, J. H. 1996, *AJ*, 111, 655
- Holtzman, J. A., et al. 1995, *PASP*, 107, 1065
- Holtzman, J. A., et al. 1996, *AJ*, 112, 416
- Hopkins, P. F., Hernquist, L., Cox, T. J., Di Matteo, T., Robertson, B., & Springel, V. 2006, *ApJS*, 163, 1
- Imanishi, M., & Alonso-Herrero, A. 2004, *ApJ*, 614, 122
- Kandalyan, R. A. 2003, *A&A*, 398, 493
- Keto, E., Jernigan, G., Ball, R., Arens, J., & Meixner, M. 1991, *ApJ*, 374, L29
- Kormendy, J. 1977, *ApJ*, 217, 406
- Korn, A. J., Maraston, C., & Thomas, D. 2005, *A&A*, 438, 685
- Kroupa, P. 2001, *MNRAS*, 322, 231
- Krügel, E., Steppe, H., & Chini, R. 1990, *A&A*, 229, 17
- Landolt, A. U. 1973, *AJ*, 78, 959
- Landolt, A. U. 1992, *AJ*, 104, 340
- Larson, R. B., & Tinsley, B. M. 1978, *apj*, 219, 46
- Malkan, M. A., Gorjian, V., & Tam, R. 1998, *ApJS*, 117, 25
- Maraston, C. 2005, *MNRAS*, 362, 799
- Maraston, C., Bastian, N., Saglia, R. P., Kissler-Patig, M., Schweizer, F., & Goudfrooij, P. 2004, *A&A*, 416, 467
- Maraston, C., Kissler-Patig, M., Brodie, J. P., Barmby, P., & Huchra, J. P. 2001, *A&A*, 370, 176
- Martin, C. L. 2005a, in *ASP Conf. Ser. 331, Extra-Planar Gas*, ed. R. Brown (San Francisco: ASP), 305
- Martin, C. L. 2005b, *ApJ*, 621, 227
- Mazzarella, J. M., & Boroson, T. A. 1993, *ApJS*, 85, 27
- Mazzarella, J. M., Bothun, G. D., & Boroson, T. A. 1991, *AJ*, 101, 2034
- Meylan, G. 2002, in *IAU Symp. 207, Extragalactic Star Clusters*, ed. D. Geisler, E. K. Grebel, & D. Minniti (San Francisco: ASP), 555
- Mighell, K. J., & Rich, R. M. 1995, *AJ*, 110, 1649
- Mihos, C. 2001, in *ASP Conf. Ser. 240, Gas and Galaxy Evolution*, ed. J. E. Hibbard, M. P. Rupen, & J. H. van Gorkom (San Francisco: ASP), 143
- Mihos, J. C., & Hernquist, L. 1996, *ApJ*, 464, 641
- Miles, J. W., Houck, J. R., Hayward, T. L., & Ashby, M. L. N. 1996, *ApJ*, 465, 191
- Miller, B. W., Whitmore, B. C., Schweizer, F., & Fall, M. 1997, *AJ*, 114, 2381
- Mulchaey, J. S., Wilson, A. S., & Tsvetanov, Z. 1996, *ApJS*, 102, 309
- Naab, T., & Burkert, A. 2003, *ApJ*, 597, 893
- Naab, T., Jesseit, R., & Burkert, A. 2006, *MNRAS*, 372, 839
- Osterbrock, D. E., & Dahari, O. 1983, *ApJ*, 273, 478
- Prouton, O. R., Bressan, A., Clemens, M., Franceschini, A., Granato, G. L., & Silva, L. 2004, *A&A*, 421, 115
- Pryor, C., & Meylan, G. 1993, in *ASP Conf. Ser. 50, Structure and Dynamics of Globular Clusters*, ed. S. G. Djorgovski & G. Meylan (San Francisco: ASP), 357
- Riffel, R., Rodríguez-Ardila, A., & Pastoriza, M. G. 2006, *A&A*, 457, 61
- Rothberg, B., & Joseph, R. D. 2004, *AJ*, 128, 2098
- Rothberg, B., & Joseph, R. D. 2006a, *AJ*, 131, 185
- Rothberg, B., & Joseph, R. D. 2006b, *AJ*, 132, 976
- Rupke, D. S., Veilleux, S., & Sanders, D. B. 2005, *ApJ*, 632, 751
- Sandage, A., & Tammann, G. A. 1975, *ApJ*, 197, 265
- Schawinski, K., et al. 2006, *Nature*, 442, 888
- Schlegel, D. J., Finkbeiner, D. P., & Davis, M. 1998, *ApJ*, 500, 525
- Schweizer, F. 1982, *ApJ*, 252, 455
- Schweizer, F. 1983, in *IAU Symp. 100, Internal Kinematics and Dynamics of Galaxies*, ed. E. Athanassoula (Dordrecht: Reidel), 319
- Schweizer, F. 1996, *AJ*, 111, 109
- Schweizer, F. 2002, in *IAU Symp. 207, Extragalactic Star Clusters*, ed. D. Geisler, E. K. Grebel, & D. Minniti (San Francisco: ASP), 630
- Schweizer, F. 2003, in *ASP Conf. Ser. 296, New Horizons in Globular Cluster Astronomy*, ed. G. Piotti et al. (San Francisco: ASP), 467
- Schweizer, F., Miller, B. W., Whitmore, B. C., & Fall, S. M. 1996, *AJ*, 112, 1839
- Schweizer, F., & Seitzer, P. 1998, *AJ*, 116, 2206
- Schweizer, F., Seitzer, P., & Brodie, J. P. 2004, *AJ*, 128, 202
- Soifer, B. T., et al. 1987, *ApJ*, 320, 238
- Springel, V., Di Matteo, T., & Hernquist, L. 2005, *MNRAS*, 361, 776
- Stetson, P. B. 1987, *PASP*, 99, 191
- Stetson, P. B. 2000, *PASP*, 112, 925
- Thomas, D., Maraston, C., & Bender, R. 2003, *MNRAS*, 339, 897
- Toomre, A., & Toomre, J. 1972, *ApJ*, 178, 623
- Trager, S. C., Worthey, G., Faber, S. M., Burstein, D., & González, J. J. 1998, *ApJS*, 116, 1
- Tremaïne, S., et al. 2002, *ApJ*, 574, 740
- Valdès, J. R., Berta, S., Bressan, A., Franceschini, A., Rigopoulou, D., & Rodighiero, G. 2005, *A&A*, 434, 149
- van der Marel, R. P., & Zurek, D. 2000, in *ASP Conf. Ser. 197, Dynamics of Galaxies: From the Early Universe to the Present*, ed. F. Combes, G. A. Mamon, & V. Charmandaris (San Francisco: ASP), 323
- van Dokkum, P. G. 2001, *PASP*, 113, 1420
- Veilleux, S., Cecil, G., & Bland-Hawthorn, J. 2005, *ARA&A*, 43, 769
- Veilleux, S., & Osterbrock, D. E. 1987, *ApJS*, 63, 295
- Véron-Cetty, M.-P., & Véron, P. 1986, *A&AS*, 65, 241
- Voit, M. 1998, in *HST Data Handbook* (Baltimore: STScI), Vol. 1, Version 3.1, Table 28.1
- White, S. D. M., & Rees, M. J. 1978, *MNRAS*, 183, 341
- Whitmore, B. C. 2003, in *A Decade of Hubble Space Telescope Science*, ed. M. Livio, K. Noll, & M. Stiavelli (Cambridge: Cambridge Univ. Press), 153
- Whitmore, B. C., Schweizer, F., Kundu, A., & Miller, B. W. 2002, *AJ*, 124, 147
- Whitmore, B. C., Schweizer, F., Leitherer, C., Borne, K., & Robert, C. 1993, *AJ*, 106, 1354
- Worthey, G., & Ottaviani, D. L. 1997, *ApJS*, 111, 377

TABLE 1  
LOG OF OBSERVATIONS OF NGC 34

Date	Telescope	Instrument <sup>a</sup>	CCD Detector	Filter	P.A. (deg)	Total Expos. (s)	Wavelength Coverage (Å)	Notes <sup>b</sup>
1995 May 13 ....	<i>HST</i>	WFPC2	Loral	F606W	282.6	500	4800–7200	<i>HST</i> Archive
2000 Sep 30 .....	du Pont 2.5 m	DC	Tek #5	<i>B</i>	1.2	6000	3850–4850	Seeing 0 <sup>''</sup> .7
				<i>V</i>	1.2	1500	4900–5800	Seeing 0 <sup>''</sup> .8
				<i>I<sub>KC</sub></i>	1.2	3600	7300–9300	Seeing 0 <sup>''</sup> .7
2002 Sep 1 .....	Baade 6.5 m	LDSS-2	SITe #1	...	351.9	1200	3650–6900	Cl. 1
					8.1	2400	3650–6900	Cl. 1, 2
2002 Oct 31 .....	Baade 6.5 m	LDSS-2	SITe #1	...	8.1	2400	3650–6850	Cl. 1, 2
2002 Nov 1 .....	Baade 6.5 m	LDSS-2	SITe #1	...	144.5	2400	3650–6850	Cl. 2, 3, 7, 13
					144.5	120	3650–6850	Nucleus

<sup>a</sup> DC = Direct camera; LDSS-2 = Low-Dispersion Survey Spectrograph 2, with 1<sup>''</sup>.03 × 330<sup>''</sup> slit.

<sup>b</sup> Cluster numbers refer to objects in Table 4.

TABLE 2  
*BVI* APERTURE PHOTOMETRY OF NGC 34

Aper. <sup>a</sup> ( <sup>''</sup> )	Radius (kpc)	<i>V</i> (mag)	$\sigma_V$ (mag)	<i>B–V</i> (mag)	$\sigma_{B-V}$ (mag)	<i>V–I</i> (mag)	$\sigma_{V-I}$ (mag)
5.....	1.03	14.818	0.001	0.725	0.002	1.325	0.001
10.....	2.06	14.117	0.001	0.676	0.002	1.194	0.001
15.....	3.10	13.749	0.001	0.633	0.002	1.126	0.001
20.....	4.13	13.551	0.001	0.608	0.002	1.096	0.001
25.....	5.16	13.436	0.001	0.595	0.002	1.084	0.001
50.....	10.3	13.224	0.004	0.580	0.005	1.085	0.004
75.....	15.5	13.168	0.008	0.579	0.010	1.090	0.009
100.....	20.6	13.140	0.014	0.581	0.018	1.088	0.015
125.....	25.8	13.115	0.023	0.586	0.028	1.086	0.024
150.....	31.0	13.098	0.032	0.589	0.039	1.087	0.034

<sup>a</sup> Aperture diameter (in arcsec).



TABLE 3  
*BVI* SURFACE PHOTOMETRY OF NGC 34

$r$ (arcsec)	$r^{1/4}$ (arcsec <sup>1/4</sup> )	$\log r$	<i>HST</i> /PC	Du Pont 2.5-m Telescope		
			$\mu_{V,HST}$ ( $\mu$ )	$\mu_{V,LCO}$ ( $\mu$ )	$B-V$ (mag)	$V-I$ (mag)
0.032	0.424	-1.492	14.44	...	...	...
0.072	0.518	-1.143	14.79	...	...	...
0.116	0.584	-0.935	15.08	...	...	...
0.161	0.633	-0.793	15.33	...	...	...
0.206	0.674	-0.686	15.66	16.60	0.784	1.792
0.297	0.738	-0.527	16.04	...	...	...
0.388	0.789	-0.411	16.43	...	...	...
0.433	0.811	-0.363	16.63	16.90	0.799	1.580
0.526	0.852	-0.279	16.91	...	...	...
0.635	0.893	-0.197	17.18	...	...	...
0.698	0.914	-0.156	17.27	17.30	0.795	1.368
0.842	0.958	-0.074	17.49	...	...	...
0.926	0.981	-0.033	17.69	17.62	0.771	1.219
1.017	1.004	0.007	17.86	...	...	...
1.18	1.042	0.072	18.08	17.95	0.711	1.161
1.44	1.095	0.158	18.26	18.22	0.683	1.131
1.70	1.142	0.230	18.46	18.44	0.657	1.118
1.96	1.183	0.292	18.65	18.64	0.662	1.108
2.22	1.221	0.346	18.89	18.77	0.667	1.100
2.48	1.255	0.394	18.91	18.89	0.653	1.085
3.01	1.318	0.479	19.10	19.08	0.631	1.045
3.65	1.382	0.562	19.38	19.32	0.630	1.019
4.41	1.449	0.645	19.69	19.61	0.613	1.001
5.34	1.520	0.728	19.90	19.83	0.553	0.955
6.46	1.594	0.810	20.24	20.16	0.517	0.922
7.82	1.672	0.893	...	20.59	0.501	0.913
9.46	1.754	0.976	...	21.09	0.493	0.943
11.45	1.839	1.059	...	21.62	0.471	0.976
13.85	1.929	1.141	...	22.16	0.516	1.026
16.76	2.023	1.224	...	22.83	0.519	1.101
20.28	2.122	1.307	...	23.41	0.537	1.144
24.54	2.226	1.390	...	24.01	0.526	1.149
29.69	2.334	1.473	...	24.85	0.557	1.192
32.66	2.390	1.514	...	25.23	0.564	1.177
39.52	2.507	1.597	...	25.78	...	...
47.81	2.630	1.680	...	26.23	...	...

NOTE. — Partial listing of surface photometry performed. Measurements at  $r \leq 1''.02$  are on *HST*/PC radius grid, with  $\mu_{V,LCO}$  (in  $\mu \equiv \text{mag arcsec}^{-2}$ ) interpolated to that grid, while measurements at  $r > 1''.02$  are on LCO radius grid, with  $\mu_{V,HST}$  interpolated to this latter grid. Estimated errors due to uncertainties in the measured sky level are small at most radii, but exceed  $\pm 0.10$  mag ( $1\sigma$ ) in  $\mu_{V,LCO}$ ,  $B-V$ , and  $V-I$  at  $r > 30''$  and reach 0.29 mag in  $\mu_{V,LCO}$ , 0.124 mag in  $B-V$ , and 0.135 mag in  $V-I$  for the last listed values.

TABLE 4  
POSITIONS AND MAGNITUDES OF THE 20 BRIGHTEST CANDIDATE CLUSTERS IN NGC 34

Object	R.A.(2000)	Decl.(2000)	$r_{\text{proj}}^{\text{a}}$		$V^{\text{b}}$ (mag)	$M_V^{\text{c}}$ (mag)	$\Delta V_{0.5-3}^{\text{d}}$ (mag)	Notes <sup>e</sup>
			(arcsec)	(kpc)				
1.....	00 11 06.997	-12 06 21.76	8.82	3.64	19.38 ± 0.01	-15.36	2.03	Sp, colors <sup>f</sup>
2.....	00 11 06.903	-12 06 31.55	6.78	2.80	20.04 ± 0.01	-14.70	1.85	Sp, colors <sup>g</sup>
3.....	00 11 06.441	-12 06 22.07	5.53	2.28	20.47 ± 0.01	-14.27	2.00	Sp
4.....	00 11 06.561	-12 06 25.54	1.92	0.79	20.65 ± 0.02	-14.09	1.75	
5.....	00 11 06.542	-12 06 26.60	0.82	0.34	20.71 ± 0.07	-14.03	2.52	Extended?
6.....	00 11 06.297	-12 06 21.88	6.56	2.71	20.77 ± 0.01	-13.97	1.94	
7.....	00 11 06.588	-12 06 24.90	2.64	1.09	20.80 ± 0.02	-13.94	1.82	Sp
8.....	00 11 06.374	-12 06 23.37	4.70	1.94	20.82 ± 0.01	-13.92	1.65	
9.....	00 11 06.491	-12 06 26.85	0.87	0.36	20.84 ± 0.06	-13.90	2.02	
10.....	00 11 06.429	-12 06 26.20	1.99	0.82	21.07 ± 0.04	-13.67	1.75	
11.....	00 11 06.314	-12 06 31.87	5.51	2.28	21.14 ± 0.02	-13.60	2.01	
12.....	00 11 06.554	-12 06 24.94	2.49	1.03	21.18 ± 0.02	-13.56	1.93	
13.....	00 11 06.707	-12 06 27.02	2.54	1.05	21.24 ± 0.02	-13.50	1.85	Sp
14.....	00 11 06.701	-12 06 17.03	10.67	4.40	21.42 ± 0.01	-13.32	1.95	
15.....	00 11 06.369	-12 06 28.53	2.70	1.11	21.44 ± 0.02	-13.30	1.69	
16.....	00 11 06.438	-12 06 28.10	1.59	0.66	21.64 ± 0.06	-13.10	1.64	
17.....	00 11 06.427	-12 06 27.50	1.60	0.66	21.74 ± 0.06	-13.00	1.88	
18.....	00 11 06.447	-12 06 30.49	3.34	1.38	21.77 ± 0.03	-12.97	1.80	
19.....	00 11 06.643	-12 06 22.77	4.91	2.03	22.00 ± 0.03	-12.74	1.85	
20.....	00 11 06.288	-12 06 24.65	4.57	1.89	22.31 ± 0.04	-12.43	1.82	

NOTE. — Units of right ascension are hours, minutes, and seconds, and units of declination are degrees, arcminutes, and arcseconds.

<sup>a</sup> Projected distance from nucleus at R.A.(2000) = 00 11 06.536, Decl.(2000) = -12 06 27.42.

<sup>b</sup> Approximate apparent  $V$  magnitude on Johnson system, transformed from F606W system as described in text.

<sup>c</sup> Absolute visual magnitude, corrected for Milky Way extinction of  $A_V = 0.089$  and computed for  $D = 85.2$  Mpc ( $H_0 = 70$  km s<sup>-1</sup> Mpc<sup>-1</sup>).

<sup>d</sup> Concentration index, which is the difference between magnitudes within apertures of 0.5 pix and 3 pix radius.

<sup>e</sup> Sp: Spectrum was obtained.

<sup>f</sup> Cluster 1:  $(B-V)_0 = 0.07 \pm 0.04$ ,  $(V-I)_0 = 0.61 \pm 0.03$ .

<sup>g</sup> Cluster 2:  $(B-V)_0 = 0.14 \pm 0.10$ ,  $(V-I)_0 = 0.71 \pm 0.13$ .

TABLE 5  
MODEL FITS TO  $BVI$  SURFACE-BRIGHTNESS PROFILES OF NGC 34

Fitted Model	Passband	Model Spheroid		Model Exponential Disk			rms Residual (mag arcsec <sup>-2</sup> )
		$\mu_{\text{eff}}$ (mag arcsec <sup>-2</sup> )	$r_{\text{eff}}$ (arcsec)	$\mu_0$ (mag arcsec <sup>-2</sup> )	$\alpha$ (arcsec)	$r_h$ (arcsec)	
Pure $r^{1/4}$ -law <sup>a</sup> ...	$B$	20.938 ± 0.057	5.88 ± 0.50	...	...	...	0.316
	$V$	20.231 ± 0.047	5.57 ± 0.38	...	...	...	0.260
	$I$	19.180 ± 0.036	5.57 ± 0.29	...	...	...	0.195
Sph + eD without hole <sup>b</sup> ...	$B$	22.408 ± 0.049	8.36 ± 0.20	19.551 ± 0.021	4.07 ± 0.04	...	0.072
	$V$	21.452 ± 0.053	7.51 ± 0.21	19.017 ± 0.027	3.80 ± 0.05	...	0.070
	$I$	19.968 ± 0.038	6.94 ± 0.13	18.557 ± 0.040	3.96 ± 0.08	...	0.093
Sph + eD with hole <sup>c</sup> ...	$B$	21.509 ± 0.026	6.36 ± 0.09	19.551 ± 0.035	3.79 ± 0.06	2.56 ± 0.08	0.064
	$V$	20.764 ± 0.033	6.20 ± 0.12	18.946 ± 0.057	3.41 ± 0.08	2.66 ± 0.11	0.066
	$I$	19.632 ± 0.027	6.29 ± 0.09	18.521 ± 0.072	3.65 ± 0.12	2.53 ± 0.17	0.089

<sup>a</sup>  $\mu(r) = \mu_{\text{eff}} + 8.325[(r/r_{\text{eff}})^{1/4} - 1]$ .

<sup>b</sup>  $\mu(r) = \mu_{\text{eff}} + 8.325[(r/r_{\text{eff}})^{1/4} - 1] + \mu_0 + 1.086(r/\alpha)$ .

<sup>c</sup>  $\mu(r) = \mu_{\text{eff}} + 8.325[(r/r_{\text{eff}})^{1/4} - 1] + \mu_0 + 1.086[(r/\alpha) + (r_h/r)^3]$ .

TABLE 6  
CLUSTER RADIAL VELOCITIES

Cluster (1)	$V$ (mag) (2)	$N_{\text{abs}}^{\text{a}}$ (3)	$c z_{\text{hel}}$ ( $\text{km s}^{-1}$ ) (4)	$\Delta v^{\text{b}}$ ( $\text{km s}^{-1}$ ) (5)
1.....	19.38	12	$5783 \pm 16$	$-85 \pm 22$
2.....	20.04	11	$5850 \pm 12$	$-20 \pm 19$
3.....	20.47	8	$5952 \pm 27$	$+80 \pm 31$
7.....	20.80	5	$5656 \pm 40$	$-210 \pm 43$
13.....	21.24	6	$5951 \pm 23$	$+79 \pm 28$

<sup>a</sup> Number of absorption lines measured.

<sup>b</sup> Line-of-sight velocity relative to nucleus,  $\Delta v = (c z_{\text{hel}} - 5870) / 1.019580$  (see text).

TABLE 7  
LICK LINE INDICES AND CLUSTER AGES

Object	$H\delta_A$ ( $\text{\AA}$ )	$H\gamma_A$ ( $\text{\AA}$ )	$H\beta$ ( $\text{\AA}$ )	Fe5015 ( $\text{\AA}$ )	Mg $b$ ( $\text{\AA}$ )	Fe5270 ( $\text{\AA}$ )	Fe5335 ( $\text{\AA}$ )	[Mg/Fe] ( $\text{\AA}$ )	$\log \tau^{\text{a}}$
Cluster 1.....	$8.2 \pm 0.3$	$7.0 \pm 0.3$	$5.3 \pm 0.1$	$1.5 \pm 0.2$	$0.5 \pm 0.2$	$0.4 \pm 0.2$	$0.5 \pm 0.2$	$0.51 \pm 0.39$	$8.16 \pm 0.05$
Cluster 2 <sup>b</sup> ...	$8.8 \pm 0.5$	$8.0 \pm 0.4$	$5.3 \pm 0.4$	$4.4 \pm 0.4$	$1.0 \pm 0.4$	$1.3 \pm 0.3$	$1.8 \pm 0.3$	$1.22 \pm 0.16$	$8.80 \pm 0.03^{\text{c}}$
Nucleus <sup>b</sup> .....	$6.6 \pm 0.4$	$4.6 \pm 0.3$	$2.9 \pm 0.2$	$3.0 \pm 0.3$	$0.6 \pm 0.1$	$0.8 \pm 0.2$	$0.3 \pm 0.2$	$0.59 \pm 0.24$	...

<sup>a</sup> Cluster age  $\tau$  expressed in years.

<sup>b</sup> Indices measured after clipping emission lines from spectrum.

<sup>c</sup> One of two possible values, the other being  $8.21 \pm 0.07$ ; for details, see § 3.5.4.

TABLE 8  
PARAMETERS OF NGC 34 (MRK 938)

Parameter	Symbol	Value
Right ascension <sup>a</sup>	$\alpha(J2000)$	00 <sup>h</sup> 11 <sup>m</sup> 06 <sup>s</sup> .54
Declination <sup>a</sup>	$\delta(J2000)$	-12° 06' 27".4
Heliocentric velocity of nucleus	$c_{\text{hel}}$	5870 ± 15 km s <sup>-1</sup>
Velocity relative to Local Group	$c_{\text{LG}}$	5961 km s <sup>-1</sup>
Distance <sup>b</sup>	$\Delta$	85.2 Mpc
Distance modulus (true) <sup>b</sup>	$(m - M)_0$	34.65 mag
Projected scale <sup>b</sup>	$s$	413 pc arcsec <sup>-1</sup>
Isophotal major diameter at $B = 25 \text{ mag}/\square''$	$D_{25}$	$\geq 107'' = 44 \text{ kpc}$
isophotal minor diameter at $B = 25 \text{ mag}/\square''$	$d_{25}$	$47''.3 = 19.5 \text{ kpc}$
Total apparent blue magnitude <sup>c</sup>	$B_T$	13.75 ± 0.01 mag
Total apparent visual magnitude <sup>c</sup>	$V_T$	13.17 ± 0.01 mag
Total apparent $I$ magnitude <sup>c</sup>	$I_T$	12.08 ± 0.01 mag
Total apparent $K$ magnitude <sup>c,d</sup>	$K_T$	9.94 ± 0.02 mag
Milky Way foreground extinction <sup>e</sup>	$A_V$	0.089 mag
Absolute blue magnitude <sup>b</sup>	$M_B$	-21.02 mag
Absolute visual magnitude <sup>b</sup>	$M_V$	-21.57 mag
Absolute $K$ magnitude <sup>b</sup>	$M_K$	-24.72 mag
Color index <sup>f</sup>	$(B - V)_{T,0}$	0.55 ± 0.02 mag
Color index <sup>f</sup>	$(V - I)_{T,0}$	1.05 ± 0.01 mag
Color index <sup>f</sup>	$(V - K)_{T,0}$	3.15 ± 0.03 mag
Infrared luminosity ( $\lambda\lambda 10\text{--}1300 \mu\text{m}$ ) <sup>g</sup>	$\log(L_{\text{IR}}/L_{\odot})$	11.54
Mass of neutral hydrogen gas <sup>b,h</sup>	$M_{\text{HI}}$	$5.3 \times 10^9 M_{\odot}$
Mass of molecular gas (from CO) <sup>b,i</sup>	$M_{\text{H}_2}$	$(7 \pm 3) \times 10^9 M_{\odot}$
Number of galaxies in NGC 34 group	$N_{\text{gal}}$	$\geq 3$
Main body:		
Apparent central surface brightness	$V_0$	14.44 mag/ $\square''$
Central velocity dispersion of stars <sup>j</sup>	$\sigma_v$	201 ± 8 km s <sup>-1</sup>
Effective radius in $V$ passband	$r_{\text{eff}}$	$6''.15 \pm 0''.10 = 2.54 \pm 0.04 \text{ kpc}$
Surface brightness at $r_{\text{eff}}$	$V_{\text{eff}} (B_{\text{eff}})$	20.08 (20.60) mag/ $\square''$
Bulge-to-disk ratio (blue) <sup>k</sup>	$(B/D)_B$	0.94
Bulge-to-disk ratio (visual) <sup>k</sup>	$(B/D)_V$	1.32
Bulge-to-disk ratio ( $I$ -band) <sup>k</sup>	$(B/D)_I$	2.7
Central exponential disk:		
Apparent semi-major axis	$a$	$\sim 8'' \approx 3.3 \text{ kpc}$
Major-axis position angle	P.A.	351°
Apparent axis ratio	$b/a$	0.72
Inclination (approx.)	$i$	44°
Approximate scale length <sup>k</sup>	$\alpha$	$4''.0 \approx 1.6 \text{ kpc}$
Maximum extent <sup>k</sup>	$r_{\text{max,eD}}$	$\geq 25'' \approx 10 \text{ kpc}$
Absolute visual magnitude <sup>k</sup>	$M_{V,0}$	-20.61 mag
Color index <sup>f,k</sup>	$(B - V)_{\text{eD},0}$	0.36 ± 0.02 mag
Color index <sup>f,k</sup>	$(V - I)_{\text{eD},0}$	0.52 ± 0.02 mag
Estimated mass (if disk 400 Myr old)	$M_{\text{eD}}$	$(2\text{--}4) \times 10^9 M_{\odot}$
Cluster system:		
Number of star clusters of $M_V \lesssim -9.3$	$N_{\text{cl}}$	$\sim 140$
Effective radius of cluster system	$r_{\text{eff,cl}}$	$2.8 \pm 0.3 \text{ kpc}$
Power-law exponent of luminosity function	$\alpha$	$-1.75 \pm 0.1$
Luminosities of 20 brightest clusters	$M_V$	-12.4 to -15.4 mag
Likely ages of two brightest clusters	$\tau$	150, 640 (or 160) Myr
Outflow:		
Mean outflow velocity of Na I	$\langle v_{\text{Na I}} \rangle$	$-620 \pm 60 \text{ km s}^{-1}$
Maximum outflow velocity of Na I	$\text{max}(v_{\text{Na I}})$	$-1050 \pm 30 \text{ km s}^{-1}$
Mean velocity shift of emission lines	$\Delta v_{\text{em}}$	$-75 \pm 23 \text{ km s}^{-1}$
Tidal tails:		
Projected length of N tail <sup>b</sup>	$r_{\text{max}}(\text{N tail})$	$92'' = 38 \text{ kpc}$
Projected length of S tail <sup>b</sup>	$r_{\text{max}}(\text{S tail})$	$63'' = 26 \text{ kpc}$

<sup>a</sup> Position of nucleus measured from *HST*/WFPC2  $V$  image.

<sup>b</sup> For  $H_0 = 70 \text{ km s}^{-1} \text{ Mpc}^{-1}$ .

<sup>c</sup> Within  $B = 26.5 \text{ mag}/\square''$  isophote.

<sup>d</sup> From Rothberg & Joseph (2004), corrected to adopted  $B$ -isophote.

<sup>e</sup> Schlegel, Finkbeiner, & Davis (1998).

<sup>f</sup> Corrected for Milky Way foreground reddening, but not internal reddening.

<sup>g</sup> Chini et al. (1992).

<sup>h</sup> From compilation by Kandalyan (2003).

<sup>i</sup> From Kandalyan (2003), Krügel et al. (1990), and Chini et al. (1992).

<sup>j</sup> Rothberg & Joseph (2006a).

<sup>k</sup> For disk without central hole; see § 3.2 and Table 5 for details.